BRNO UNIVERSITY OF TECHNOLOGY

VYSOKÉ UČENÍ TECHNICKÉ V BRNĚ

FACULTY OF MECHANICAL ENGINEERING

FAKULTA STROJNÍHO INŽENÝRSTVÍ

INSTITUTE OF PHYSICAL ENGINEERING

ÚSTAV FYZIKÁLNÍHO INŽENÝRSTVÍ

DYNAMIC IN-SITU EXPERIMENTS UTILIZING PROBE MICROSCOPY

DYNAMICKÉ IN-SITU EXPERIMENTY S VYUŽITÍM SONDOVÉ MIKROSKOPIE

MASTER'S THESIS

DIPLOMOVÁ PRÁCE

AUTHOR   Bc. Marek Patočka
AUTOR PRÁCE

SUPERVISOR   doc. Ing. Miroslav Kolíbal, Ph.D.
VEDOUCÍ PRÁCE

BRNO 2024

Assignment Master's Thesis

Institut: Institute of Physical Engineering
Student: **Bc. Marek Patočka**
Degree programm: Physical Engineering and Nanotechnology
Branch: no specialisation
Supervisor: **doc. Ing. Miroslav Kolíbal, Ph.D.**
Academic year: 2023/24

As provided for by the Act No. 111/98 Coll. on higher education institutions and the BUT Study and Examination Regulations, the director of the Institute hereby assigns the following topic of Master's Thesis:

Dynamic in–situ experiments utilizing probe microscopy

Brief Description:

Probe microscopy is an established technique for measurement of local physical characteristics of different samples. Apart from roughness it allows to measure conductivity, electric potential etc. Current research trends focus on dynamic in–situ experiments that mimic real process conditions in e.g. catalysis, electronics or batteries. Student will focus on selected applications, and he is expected to demonstrate the capabilities of SPM Litescope for dynamic experiments.

Master's Thesis goals:

1. Propose suitable experiments, focusing preferentially on utilizing SPM for battery research, power electronics and also dynamic experiments at elevated temperature.
2. Design appropriate technical solution and demonstrate its function.
3. Critically discuss the obtained results.

Recommended bibliography:

ZHANG, Z. et al., Capturing the swelling of solid-electrolyte interphase in lithium metal batteries. Science, r. 2022, č. 375, s. 66-70.

JI, J.-Y. et al., Homogeneous Lateral Lithium Intercalation into Transition Metal Dichalcogenides via Ion Backgating. Nano Letters, r. 2022, č. 22, s. 7336-7342.

YAMAGISHI, Y. et al., Molecular-Resolution Imaging of Interfacial Solvation of Electrolytes for Lithium-Ion Batteries by Frequency Modulation Atomic Force Microscopy. Nano Letters, r. 2022, č. 22, s. 9907-9913.

ZHU, C. et al., Understanding the evolution of lithium dendrites at Li6.25Al0.25La3Zr2O12 grain boundaries via operando microscopy techniques. Nature Communications, r. 2023, č. 14, s. 1300.

Deadline for submission Master's Thesis is given by the Schedule of the Academic year 2023/24

In Brno,

L. S.

_____   _____
prof. RNDr. Tomáš Šikola, CSc.   doc. Ing. Jiří Hlinka, Ph.D.
Director of the Institute   FME dean

Summary

In this thesis, several case-studies of dynamic in-situ scanning probe microscopy experiments are presented. First, the electrodeposition of lithium in a solid state battery without a positive electrode is investigated. This experiment is followed by a similar measurement in which MXene particles are employed as a positive electrode material. The second part of the thesis deals with the graphene-on-liquid-metal system. An investigation into the presence of a meniscus surrounding the graphene flakes is presented.

Abstrakt

V této práci je uvedeno několik případových studií dynamických in-situ experimentů s využitím skenovací sondové mikroskopie. Nejprve je zkoumána elektrodepozice lithia v baterii s pevným elektrolytem bez kladné elektrody. Na tento experiment navazuje obdobné měření, při kterém jsou jako materiál kladné elektrody použity částice MXene. Druhá část práce se zabývá grafenem plovoucím na kapalném kovu. Je zde prezentováno zkoumání přítomnosti menisku okolo grafenových vloček.

Keywords

In-situ, Atomic force microscopy, Graphene, Solid state batteries, MXene, LiteScope

Klíčová slova

In-situ, Mikroskopie atomárních sil, Grafen, Baterie s pevným elektrolytem, MXene, LiteScope

I declare that this thesis is my original work and that I have written it independently under the supervision of doc. Miroslav Kolíbal using the information sources listed in the bibliography. AI tools have been used solely as assistive tools in order to improve the wording of the text.

Bc. Marek Patočka

Contents

1 Introduction

Scanning probe microscopy (SPM) has evolved massively since its invention less than 50 years ago. It has found its niche in many branches of science, ranging from biology to semiconductor research and quantum physics. It is a unique tool which enables us to access nanoscale features with relatively simple instrumentation. It is also incredibly versatile as a single device can be used to perform basic topography measurements as well as other, more advanced, analyses. Lastly, some properties of the samples (e.g. stray electric field) can only be explored with SPM techniques.

However, probe microscopies are often viewed as slow and only viable for ex-situ analyses. Unlike most optical microscopies or transmission electron microscopy, the SPM is a family of *scanning* microscopies, which means that the images are captured line-by-line. The scanning time is usually on the order of minutes. Understandably, unlike, for example, electron microscopy [1], SPM is not widely used to image dynamic processes. Although high-speed topography measurements are becoming increasingly common [2], they are still a marginal technique, and even they cannot match the image acquisition rate of other techniques. Nevertheless, many significant processes in the microscopic world occur on a time scale that can be documented using an SPM. For example, ion transport in a battery is a continuous process during which ions migrate from one electrode to the other. Apart from the extreme case of short-circuiting and thermal runaway, this process occurs at a rate that can be recorded by an ordinary IV spectroscopy in the SPM.

Another significant point is that interesting processes usually do not occur at room temperature. Currently, there is a significant focus on the need to conduct experiments in-situ and under special conditions. This often results from the delicate nature of the samples, as certain specimens deteriorate, unless they are kept in specific environments. The examples are, once again, certain air-sensitive battery materials. On the other hand, some specimens are of interest only if they are heated to high temperatures. An example of such a sample, which is also shown in this thesis, is graphene floating on top of molten gold.

The thesis is divided into three chapters. The first one, which is also the briefest, outlines the analytical techniques utilised in the following chapters. It mainly deals with the theory of SPM and Scanning Electron Microscopy (SEM). The SPM-in-SEM microscope LiteScope is also introduced as it is the most important instrument for this work.

The second chapter touches on the topic of energy storage, different types of batteries, their pros and cons, and the emerging technology of solid state batteries. After briefly mentioning an attempt at atomic force microscopy measurement inside a liquid electrolyte, two sections devoted to experiments with lithium transport through a solid state electrolyte follow. A successful electrodeposition of lithium pillars is presented. The pillars were deposited by driving the lithium ions from an InLi negative electrode to the tip. Subsequently, the same experiment is repeated, this time with the intent of exploring if the migrating ions can be embedded inside MXene particles which are employed as positive electrodes.

The third chapter deals with the graphene-on-liquid-metal system. Specifically, it addresses the question of whether graphene flakes floating on liquid gold can interact with each other through capillary forces. In order to do so, graphene is grown via chem-

ical vapour deposition and then the topography is investigated with the atomic force microscopy.

Overall, this thesis aims to explore possible use-cases for the SPM-in-SEM technique. Therefore, it is separated into individual sections that do not necessarily relate to each other. However, I hope that the underlying goal of exploring possible future applications of SPM-in-SEM remains apparent at all times.

2 Analytical Techniques

The following chapter describes the analytical techniques used in this thesis. It starts with scanning probe microscopy (SPM) and its subtypes – atomic force microscopy (AFM) and conductive AFM (C-AFM). Another important technique, the scanning electron microscopy (SEM), is described in the next section.

2.1 Scanning Probe Microscopy

The SPM is a family of imaging techniques used for surface imaging. It covers a wide range of microscopies that can provide information about surface topography (scanning tunnelling and atomic force microscopies), magnetic and electric properties (magnetic, electric and Kelvin probe force microscopies), conductivity (conductive AFM) and many other qualities of the sample. The basic principle of SPM is the utilisation of a sharp tip located at the end of a long beam called *cantilever*. The whole device is often referred to as *probe*.

Even advanced techniques usually provide information about the sample topography. The probe scans the surface line by line and some sort of feedback signal (e.g. cantilever deflection) is acquired which is proportional to the tip-sample distance. This signal is kept constant (this target value is called *setpoint*) by an electronic controller that moves the sample (or less often the probe) up and down. If the vertical (z) position of the sample is mapped to individual horizontal (x, y) positions of the probe, it is possible to obtain a map showing the topography of the sample. The basic schematics are shown in Figure 2.1 [3].
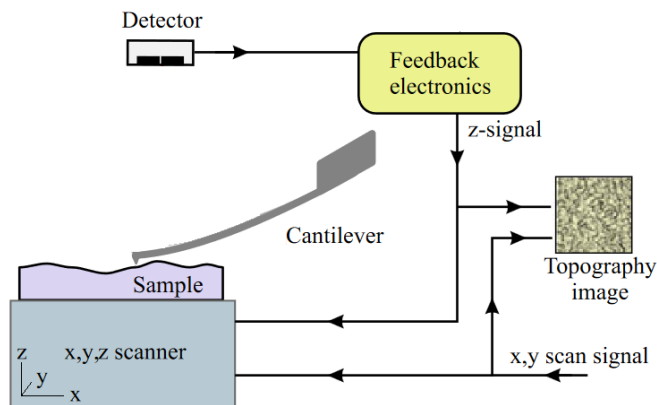
Figure 2.1: Topography acquisition by a Scanning Probe Microscope. The probe is stationary while the sample moves in x and y directions. The tip-sample distance is kept constant by moving the sample in the z direction. Adapted from [3].

2.1.1 Atomic Force Microscopy

The AFM is probably the most well-known and widely used SPM technique. It utilises forces between the sample and the tip to reconstruct the surface topography. These forces can be attractive as well as repulsive and dominate at different distances (short-

versus long-distance interactions). Tip-sample interactions are a wide topic, and even after neglecting capillary (a small drop of water from air humidity forms around the tip during scans under ambient conditions) or electrostatic forces and only focusing on van der Waals forces, the system is still very complex. However, there is a simplification. It can be assumed that the (usually oscillating) tip approaching a surface is first attracted by it (this effect is further neglected) and then repulsed by it. Due to the repulsion, the oscillation amplitude of the cantilever decreases and its resonance frequency increases (see Figure 2.2). This change in resonance frequency is called *frequency shift* Δf. It is possible to use this frequency shift as a feedback signal. Microscopes that use this type of feedback are designated as operating in *frequency modulated tapping regime*. Alternatively, the deflection of a non-oscillating cantilever can be used as the feedback signal. AFM imaging performed in this manner is dubbed *contact AFM*. Images obtained by the contact AFM usually suffer from a worse resolution than those from a tapping AFM and the specimen is more likely to suffer damage as the tip-sample forces are larger.
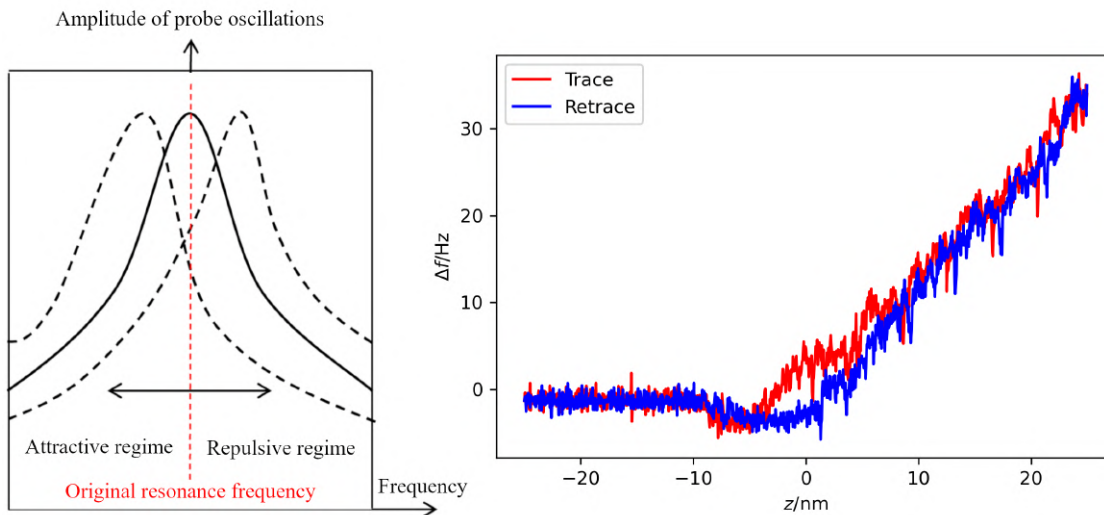

Figure 2.2: The shift of the resonance frequency peak caused by attractive and repulsive forces after neglecting the decrease in amplitude (on the left) and the dependency of the frequency shift (Δf) on the sample position (z) measured with the LiteScope microscope (on the right). Left Figure adapted from [5].

2.1.2 Conductive Atomic Force Microscopy

The conductive AFM (C-AFM) is a technique used for electronic characterisation of nanostructures and surfaces. Initially, C-AFM might seem akin to the scanning tunnelling microscopy (STM), yet significant distinctions exist. In the STM, the current between the probe and the sample is the signal used to control the vertical position of the tip (the desired current is the setpoint). In the C-AFM, the vertical position of the tip is controlled in the same manner as in a common AFM. The microscope is operated in the contact AFM mode, therefore the desired cantilever deflection is the setpoint. The reason why we use the contact mode is that a continual electric connection between the tip and the sample is necessary. It is so because during a C-AFM measurement there is a voltage difference between the tip and the sample and the flowing current is measured. During a single scan, it is possible to obtain information about the sample's topography and its

conductive properties. It is clear that the quality of contact between the probe and the sample significantly influences the magnitude of the measured current [4].

2.2 Scanning Electron Microscopy

Another vital instrument utilised in the practical part of this thesis is the scanning electron microscope (SEM). In an SEM, a narrow beam of electrons, nanometres in diameter, is extracted from a cathode (also known as an electron gun) and directed by a series of optical elements to the specimen. The observed material then either scatters some of these electrons back (so-called backscattered electrons, BSEs), or the impact of the primary electrons causes the emission of electrons from the specimen (so-called secondary electrons, SEs) [7]. This operation principle is also outlined in Figure 2.3.
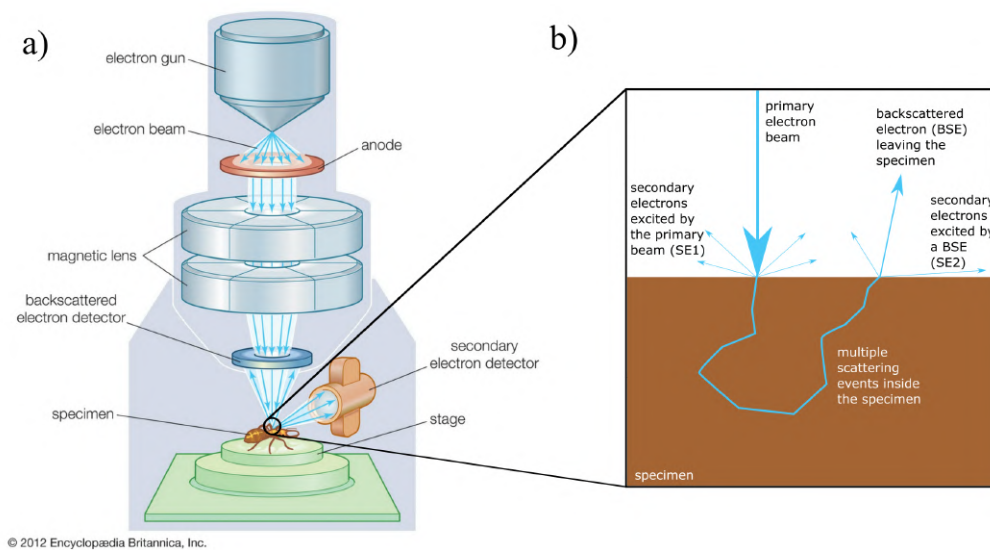

Figure 2.3: A schematic of the Scanning Electron Microscope and the electron-matter interactions. **(a)** An electron is emitted from the electron gun, accelerated by the anode, and directed by the magnetic lenses until it eventually hits the specimen. **(b)** In the specimen, primary electrons excite secondary electrons (SEs) and sometimes scatter back as backscattered electrons (BSEs). Part **(a)** reproduced from [6].

2.2.1 Focused Ion Beam

A special tool that can be fitted to an SEM is the Focused Ion Beam (FIB). It is essentially another column mounted to the SEM at an angle that accelerates ions instead of electrons. The beams from both columns are directed towards the sample. The ions sputter atoms on the surface of the sample, and this effect allows for nanoscale removal of the sample material. The impacting ions also cause the emission of secondary electrons, which can be detected using conventional detectors. Traditionally, gallium-based liquid metal ion sources had been used in FIB systems; however, more versatile, less contaminating and more expensive plasma sources, which are capable of providing much higher ion currents, have recently found their way to the mainstream use [8, 9].

2.2.2 Gas Injection System

A dual-beam (SEM and FIB) microscope is usually equipped with a gas injection system (GIS), which enables a small amount of gas (on the order of milipascals) to be introduced into the microscope chamber. This gas (often dubbed a *precursor*) is usually an organic substance containing an element that we want to deposit on the specimen surface. The precursor molecules adsorb to the surface while the electron or ion beam illuminates it and causes SE emission. The SEs cause the dissociation of the precursor molecules, releasing the deposited atom, which stays on the surface as the reaction products are pumped out. This added material can be used to connect two objects together in a process similar to welding. The deposited material is not of high purity, contains a large amount of other elements and does not have the same electrical properties as a pure metal in case of metal deposition [8].

2.3 LiteScope

LiteScope (see Figure 2.4) is an AFM microscope developed by the NenoVision company dedicated for the integration into an SEM microscope. The main advantage of LiteScope is the possibility of simultaneous observation of the sample by an SEM and the SPM. This is often crucial for sample navigation. LiteScope performs scanning by moving the sample with the probe being stationary. This setup is called *scanning-sample*.
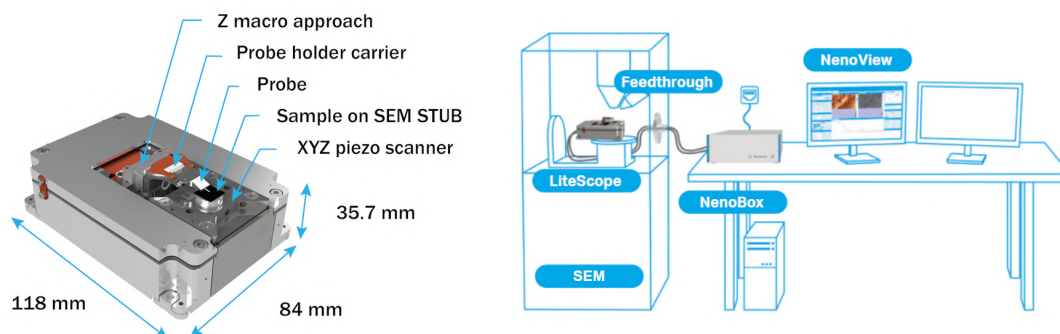

Figure 2.4: The LiteScope SPM-in-SEM (on the left). The microscope can be integrated into an SEM microscope (this setup is shown on the right) and connected to its controller NenoBox through a feedthrough. The device is controlled by a software called NenoView. Reproduces from [10].

In this thesis, two types of LiteScope compatible SPM probes have been employed. The first type is the Akiyama probe (see Figure 2.5a) which is always operated in the frequency modulated tapping regime. The probe is based on a quartz tuning fork which drives the tip and therefore cannot be operated in other modes such as contact AFM or amplitude modulated tapping AFM. The apex of the probe is visible from the top, eliminating the need to tilt the microscope in the SEM for tip observation [11]. The second type of probe is the NenoProbe Conductive (the NPC probe, see Figure 2.5). It is a self-sensing SPM probe with a platinum-coated tip. In the SEM, the tip of the probe is visible only if the LiteScope is tilted by more than $35°$ about the axis of the probe cantilever. The NPC probe is equipped with a Wheatson bridge (see Figure 2.6) based sensor to detect

cantilever deflection. Some of the bridge resistors (one from each branch) are lithograph-ically patterned on the cantilever. Because the bending of the cantilever stretches these resistors, their resistance changes when the cantilever bends, thus "throwing the bridge off balance". The bridge is also inherently unbalanced before the start of the measure-ment because of manufacturing inaccuracies. It needs to be balanced by applying certain external offset voltage (i.e. the reading on the voltmeter must be 0 V before the approach to the sample).
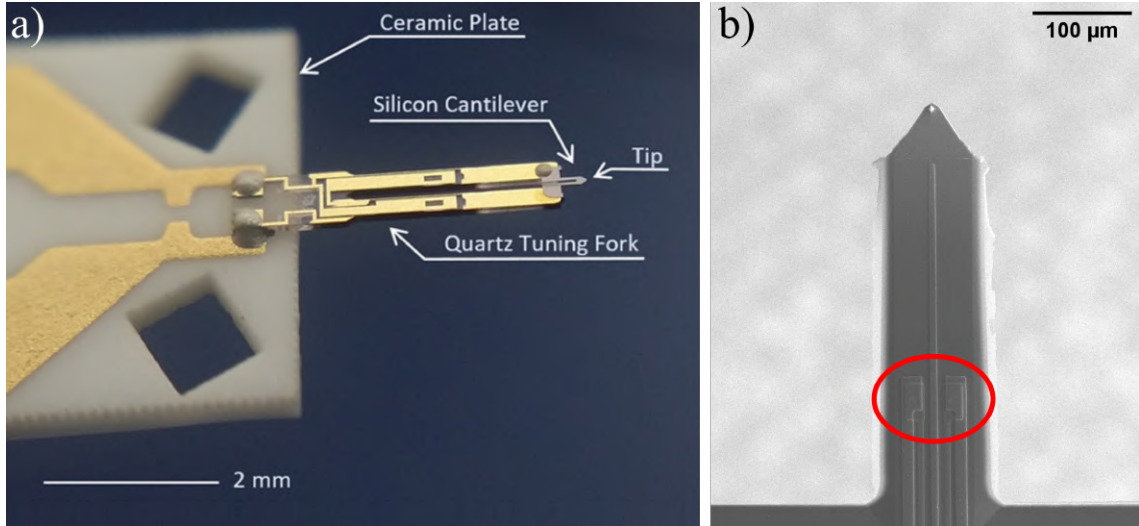

Figure 2.5: The SPM probes utilised in this thesis. **(a)** The Akiyama probe (an optical microscope image). Alternating current is supplied to electrical contacts patterned on the tuning fork to drive its oscillations. The tip oscillates in the direction perpendicular to the ceramic plate. The probe resonance frequency is approximately 40 kHz, the stiffness is approximately 5 N/m and the tip radius is smaller than 15 nm. **(b)** The NPC probe with cantilever length 420 µm (an SEM image). Probes with different cantilever lengths are also available and were used in the thesis. The stiffness and resonance frequency of the probe strongly depend on this length. The red ellipse marks the two sensing piezoresistors on the probe. The tip is coated with platinum and the tip radius is smaller than 15 nm. Panel (a) reproduced from [11].
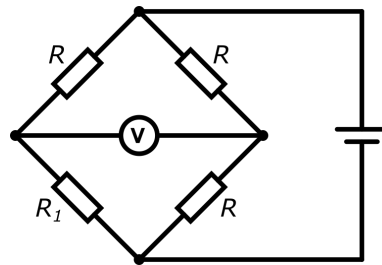

Figure 2.6: The Wheatson bridge. The circuit consists of four resistors. If the resistance of all resistors is the same (i.e. $R = R_1$), the voltmeter in the middle reads 0 V. If the resistance of one of the resistors changes (i.e. $R \neq R_1$), the reading on the voltmeter changes too. The drawing has been created in Falstad Circuit Simulator Applet.

3 Batteries

This chapter begins with an examination of the operating principle of the lithium-ion (Li-ion) cell. Next, an alternative design that uses lithium, known as a lithium-metal (Li-metal) battery, is presented. Lastly, the possibility of using a different kind of electrolyte, the solid electrolyte, is investigated. This type of electrolyte is currently gaining significant attention because of its promise of enhanced safety and chemical stability.

3.1 Operating principle of batteries

The operation of batteries is based on reversible electrochemical reactions that involve the transfer of material between two electrodes. These are commonly called *cathode* and *anode.* However, since these terms are reversed during charging and discharging,[1], we will use the terms *positive electrode* and *negative electrode* as in [13].

The charging procedure (see Figure 3.1) requires a transfer of material from the positive electrode to the negative electrode. As cations (in the case of Li-ion batteries Li^+) move from the positive electrode to the negative electrode through the electrolyte during charging, electrons are driven by an external source in the same direction in the external circuit, ensuring the electrical neutrality of both electrodes [14]. The discharge process involves the transition to a lower-energy state (of the whole system), with ions that were located in the negative electrode moving back to the positive electrode. Electrons that traverse the external circuit are capable of performing useful work [14].

Both electrodes are separated by an electrolyte, which is an ion-conductive material (liquid or solid) with minimal electron conductivity. Electrolytes do not store energy, but they are still a vital component of a cell, making up 8 - 15 % of its mass [13]. Electrolytes are often the determining factor for cell safety and the development of new chemistries (batteries with new electrode materials) is often dependent on finding a suitable electrolyte. Electrolytes often determine the thermal stability and lifetime of the cell [13].

3.2 Physical quantities describing a battery

This section briefly outlines some electrochemical quantities that are important in the field of battery research. As mentioned previously, ions in a discharging battery move from the negative electrode towards the positive one. A voltage is created between the electrodes in the external circuit that drives the electrons through the circuit. As a first approximation, this voltage (theoretical standard cell voltage, denoted as U^0) can be

---

[1] *Cathode* is defined as the electrode where reduction occurs [12]. Usually, this term is assigned to battery poles when the battery is discharging.
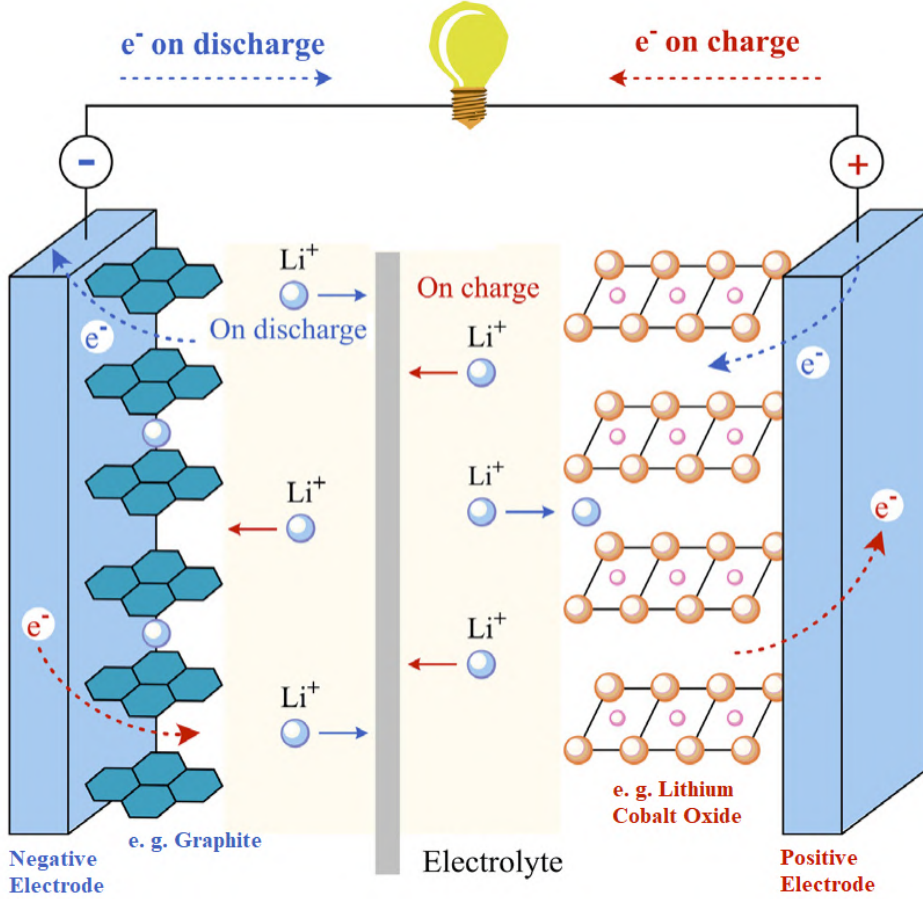
Figure 3.1: Charge (in red) and discharge processes (in blue) in Li-ion battery. Li$^+$ cations are shown to move from the positive electrode to the negative electrode while charging and in the opposite direction while discharging. Adapted from [14].

calculated from standard electrode potentials (SEPs)[2] ($U^0_{electrode}$)[3] of electrodes undergoing a known redox reaction as

$$U^0 = U^0_{positive\ electrode} - U^0_{negative\ electrode}. \tag{3.1}$$

The values of $U^0_{electrode}$ for some important reactions are listed in Table 3.1. However, a real cell is not in the standard state. Correction of U^0 for the temperature and chemical activities of the electrodes is possible using the Nernst equation. The Nernstian potential U is given by

$$U = U^0 - RT \ln Q, \tag{3.2}$$

where $R = 8.31\,\mathrm{J/kmol}$ is the gas constant, T is the thermodynamic temperature, and Q is the chemical quotient of the reaction which can be calculated as $Q = a_{products}/a_{reactants}$, where a is the chemical activity. It is important to note that a changes with the concentration of reactants and therefore Q and U change during the discharge (or charge) of the

---

[2]IUPAC defines SEP against the standard hydrogen electrode ($U^0_{2H^+ + 2e^- \longrightarrow H_2} = 0\,\mathrm{V}$) as "*The value of the standard emf of a cell in which molecular hydrogen under standard pressure is oxidized to solvated protons at the left-hand electrode [15].*" Other definitions, where SEP of another reaction is zero, are possible too.

[3]SEP is often denoted as E^0, but in this text, this denotation could be mistaken for other quantities, such as energy, and therefore denotation U^0 is used.

Redox reaction	U^0 (V) at $T = 298\,\text{K}$	C^m (mAh/g)
$\text{Li}^+ + \text{e}^- \longrightarrow \text{Li}$	-3.10	3861
$\text{Na}^+ + \text{e}^- \longrightarrow \text{Na}$	-2.71	1166
$\text{Mg}^{2+} + 2\text{e}^- \longrightarrow \text{Mg}$	-2.36	2205
$2\text{H}^+ + 2\text{e}^- \longrightarrow \text{H}_2$	0.00	26591
$\text{F}_2 + 2\text{e}^- \longrightarrow 2\text{F}^-$	2.87	1411

Table 3.1: Standard electrode potentials and specific capacities for reductions of certain selected elements. Adapted from [16] and [17].

battery. The real voltage, which we can measure on a functioning cell, is also affected by several other phenomena. For example, the voltage drops with increasing energy output of the battery in the so-called *IR drop*. This drop gives rise to an effect known as internal resistance (a real voltage source can be split into an ideal source and a resistor connected serially to each other). Other effects related to battery's inner working usually cause further decrease in voltage. It is desirable for the cell voltage to remain constant during discharge [16].

With this knowledge, the positive electrode can be defined as the electrode with a higher SEP and the negative electrode as the one with a lower SEP. For obvious reasons, $U^0_{positive\ electrode}$ is generally higher than zero in this convention (against the standard hydrogen electrode), while $U^0_{negative\ electrode}$ is lower. However, this "rule of thumb" does not always hold, as many different factors determine the choice of electrode materials [17].

Another, perhaps the most important, parameter of batteries is their capacity. However, it is first necessary to define several quantities that describe the materials of electrodes. The first quantity defines the number of electrons (the amount of charge) that the material can provide per unit of mass in a given redox reaction. This value is called s specific capacity (denoted as C^m, measured in mAh/g) and is defined as

$$C^m = \frac{z \cdot F}{M_{active\ material}}, \tag{3.3}$$

where $F = 96\,485\,\text{C/mol}$ is the Faraday constant, z is the number electrons provided by the positive electrode material in the reaction and $M_{active\ material}$ is the molar mass of the active material. Specific capacities of selected materials are again shown in Table 3.1 [17].

The capacity of a whole cell can also be defined. The operation principle of modern batteries was briefly touched upon in Section 3.1. Their electrodes utilise the intercalation of ions into the structure of electrodes (e.g. lithium in LiCoO_2 positive electrode). Understandably, the molar mass and specific capacities of the electrodes change during charging and discharging. This change also depends on the efficiency of ion transport between the electrodes (whether all ions are mobile). The specific capacity of the whole charged cell is defined as

$$C^m_{charged\ cell} = \frac{C^m_{charged\ positive\ electrode} \cdot C^m_{charged\ negative\ electrode}}{C^m_{charged\ positive\ electrode} + C^m_{charged\ negative\ electrode}}. \tag{3.4}$$

The capacity of the whole cell is therefore smaller than the capacities of the individual electrodes [17].

At this point, the energy released when a single electron is moved from the positive to the negative electrode can be determined (using U^0, as a cell in the standard state is considered

13

for simplicity) and the number of electrons that can be transferred in this manner (using C^m). It is therefore time to define the gravimetric energy density E^m of an electrode material. However, U^0 is defined between two electrodes. According to the customs of electrochemistry, it is defined here against a hydrogen electrode ($U^0_{negative\ electrode} = 0\,\mathrm{V}$). Then

$$E^m = U^0 \cdot C^m = (U^0_{positive\ electrode} - U^0_{negative\ electrode}) \cdot C^m = U^0_{positive\ electrode} \cdot C^m \quad (3.5)$$

and E^m is usually expressed in Wh/kg. Notice that E^m of elements with $U^0 < 0\,\mathrm{V}$ (e.g. fluorine) is negative in this convention. It is crucial to emphasise that this value cannot be used unquestioningly in computations. It is always necessary to consider the specific redox reaction that takes place [17].

Understandably, there are changes in batteries during (dis)charging which have been neglected in this text. In real-world calculations, it is necessary to consider all these effects. However, that topic is beyond the scope of this thesis. A simplified view on the operating principle of batteries, electrodes, and cell capacities has been developed, and now it is time to look at some examples of commercially successful batteries and emerging technologies.

3.3 Lithium-ion batteries

Li-ion batteries were commercialised in 1991. In the initial designs, $LiCoO_2$ was used as the positive electrode material and certain carbonaceous materials (i.e. hard carbon or mesophase graphite) as the negative electrode. A solution of propylene carbonate with lithium salts (e.g. $LiPF_6$ or $LiBF_4$) was used as an electrolyte. The primary benefit of these materials is their stability under atmospheric conditions [18].

Since its introduction in 1991, $LiCoO_2$ has been joined by a variety of other materials used in positive electrodes. They often decrease the molar fraction of cobalt by replacing it with other cheaper metals, i.e. $LiNi_{1/3}Mn_{1/3}Co_{1/3}O_2$ (NMC class of materials) or $LiNi_{0.8}Co_{0.15}Al_{0.05}O_2$ (NCA class). Several new materials, such as $LiFePO_4$, have also found their niche [13, 18]. In recent years (as of 2023) we have seen a switch from cobalt-based electrodes to cheaper nickel- and manganese-based electrodes [13]. Cobalt extraction is expensive, damaging to the environment, and it has been linked to human rights abuses [19]. Electrodes based on NMC type materials are expected to dominate the market in this decade. Particularly, NMC622 ($LiNi_{0.6}Mn_{0.2}Co_{0.2}O_2$) and NMC811 ($LiNi_{0.8}Mn_{0.1}Co_{0.1}O_2$) are anticipated to be successful and help reduce the cobalt consumption [20].

A less dramatic progress has been made in the area of negative electrodes. Hard carbon and mesophase graphite, predominantly used in the 1990s, have been replaced mainly by modified natural graphite. Natural graphite is theoretically a great material for negative electrodes. Unlike hard carbon, it offers a flat discharge curve (see Figure 3.2), which means that the battery voltage remains mostly constant during discharge. This is advantageous for some applications (e.g. cell phones). Another, perhaps even more important, advantage is the lower price of graphite. However, the chemical reactivity of natural graphite did not allow it to be used with traditional electrolytes. For example, when used with the propylene carbonate mentioned above, it causes the electrolyte to
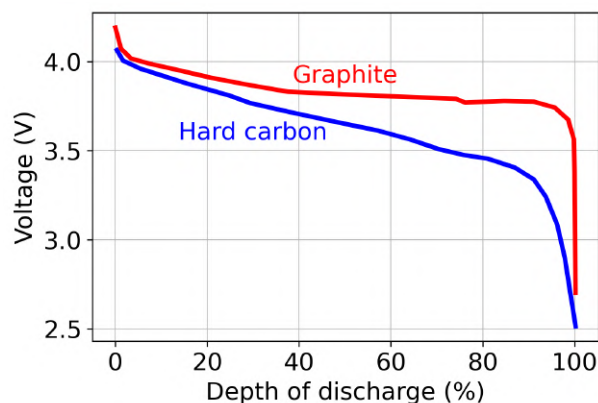
Figure 3.2: Comparison of discharge curves between graphite (red) and hard carbon (blue) when used against $LiCoO_2$ positive electrode. Depth of discharge can be thought of as *100 % - the percentage of useful energy remaining stored in the battery*. Based on [18].

decompose. The graphite surface must be coated with a carbon layer (thereby forming modified natural graphite), preventing this reaction [18].

Lithium titanate has been another material used for negative electrodes. It provides a reliable performance even at low voltages, as the electrode-electrolyte interface does not suffer from significant deterioration. However, this type of cell provides only about half the specific capacity (energy per mass) and less than two thirds of the discharge voltage of graphite-based cells. Combined with higher cost, these problems have prevented lithium titanate from replacing graphite [13].

For reasons previously mentioned, much attention is currently devoted to the development of novel negative electrode materials. Various lithium compounds, such as LiAl, $Li_{21}Sn_5$, $Li_{21}Si_5$, etc., were proposed, but their main disadvantage is their large volume expansion during charging [18]. Another new trend is the use of silicon oxide in negative electrodes, beginning with small amounts in 2013. It is expected that the first batteries with major silicon content will be available by 2025 (as of 2023) [13].

Improvements in the design and streamlining of the manufacturing process have led to a general increase in the energy density, lifetime, and safety of Li-ion cells. Production volumes are increasing steadily and are expected to continue to do so, while these combined developments have caused the price of Li-ion batteries to plummet (see Figure 3.3) [13, 18, 19].

3.4 Lithium-metal batteries

At first glance, it may appear that Li-ion and lithium-metal (Li-metal) batteries are quite alike. The main similarity is the utilisation of Li^+ ion transfer. However, there are some significant distinctions between them. Li-metal batteries utilise pure metallic Li as a negative electrode. Some exotic solutions have been proposed for the positive electrode. They include sulphur and air (respectively, O_2). The theoretical specific energy density of Li-O_2 and Li-S combinations is much higher than that of Li-ion batteries, with Li-O_2 reaching 3505 Wh/kg and Li-S 2600 Wh/kg, compared to the approximate 350 Wh/kg of Li-ion batteries [22]. Safety concerns have hindered the development of these
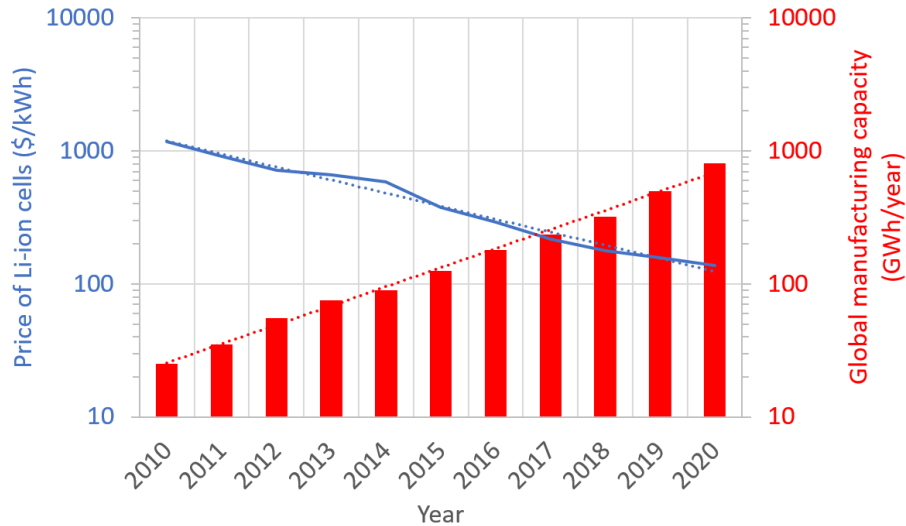
Figure 3.3: Decline of Li-ion battery cost and increase in global manufacturing capacity. Based on [21].

batteries as they are, for example, susceptible to dendrite growth (thin tree-like structures growing from the negative electrode). These dendrites short-circuit the electrodes, causing spontaneous fires. There are also concerns about *swelling* (a large volume change during charging/discharging) and electrolyte stability. Li-metal batteries are being thoroughly studied in order to address these issues. Despite extensive efforts, a breakthrough is yet to come [22].

3.5 Solid-state batteries

Thus far, the primary focus of the thesis has been on the electrode materials; however, it is equally important to consider the electrolyte, which serves as the medium for ion movement between the electrodes. The electrolyte can prevent or accelerate dendrite growth, shorten or prolong battery life, drastically affect cell safety, limit cell temperature stability, etc. For many years, electrolytes based on $LiPF_6$ dissolved in organic solvents (e.g. ethylene carbonate) have been the industrial standard [13].

In pursuit of safer, more economical, and higher capacity batteries, scientists have started paying more attention to other types of electrolytes. Research is being conducted extensively on solid state electrolytes (SSEs), which are utilised in solid state batteries (SSBs). According to [13], they are "*arguably among the most hyped technologies of this decade so far.*"

In principle, SSEs operate in a manner similar to that of liquid electrolytes (the working principle is described in Figure 3.4). Their purpose is to provide an ionically conductive conduit between the electrodes. Although some older types of SSEs poses limited ionic conductivity, allowing them to be used only in thin film cells, newly developed electrolytes allow for cells with dimensions similar to those of cells with a liquid electrolyte [25]. SSEs are less susceptible to fire than liquid electrolytes, perform better at lower temperatures, and have a longer lifespan and faster charging. Since they replace a liquid solution with an inherently denser material, it could be expected that the specific energy of an SSB

is lower; however, the opposite is the case. As discussed above, Li-metal and sodium-metal (a possible novel alternative to Li-metal batteries) batteries have significant issues with dendrite growth. The use of an SSE together with these negative electrodes can impede dendrite formation [25]. Some obstacles still need to be addressed before a full commercialisation of SSBs. These include undesired electronic conductivity, as only ions should pass through the electrolyte, unsatisfactory mechanical properties, and interfacial resistance between the electrolyte and the electrodes [25].
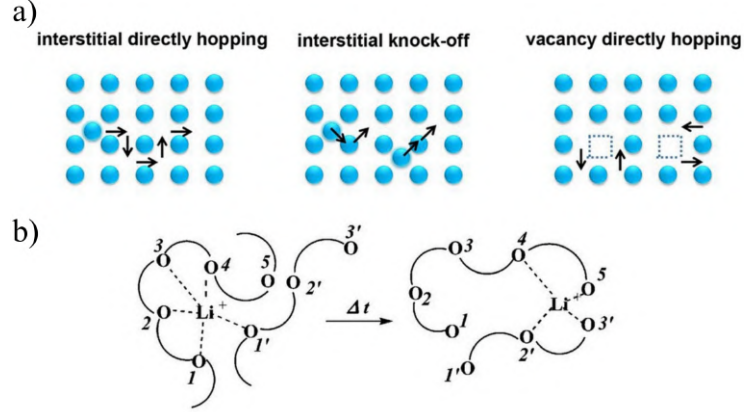

Figure 3.4: Operating principle of SSE's ionic conduction. **(a)** In crystalline media like some ceramic electrolytes, ions act as defects and their movement can be described as a defect motion. **(b)** In polymer electrolytes, ions move by *hopping* from one polymer site to another. Reproduced from [24].

3.6 AFM inside a liquid electrolyte

In [26], the authors present a fluid AFM measurement within a working Li-ion battery. They were able to observe the growth of the solid electrolyte interface (SEI), which is a layer forming between the liquid electrolyte and the negative electrode. I attempted to perform a similar measurement with LiteScope and the Akiyama probe. Because these measurements necessitate working inside a liquid electrolyte, the first step was an investigation into the possibility of performing AFM scans inside the liquid environment. Since the quartz tuning fork of the Akiyama probe has electrical contacts patterned on it, only the tip of the probe can be submerged in the electrolyte (see Figure 3.5a). I performed this test by placing a small droplet of electrolyte on a lithographically etched AFM test grating dubbed TGQ1 (see Figure 3.5b for specifications) [27], followed by inside it. This grating has a square pattern with a period of $3\,\mu m$. The electrolyte used in this section is a mixture of an ionic liquid[4] compatible with high vacuum (therefore compatible with SEMs) and Lithium bis(trifluoromethanesulfonyl)imide (LiTFSI) salt (sample courtesy of Ing. Ondřej Klvač). The same salt was used in [26], as the authors claim that lithium hexafluorophosphate ($LiPF_6$), which is today an industrial standard, causes the production of HF in the cell and degradation of the probe. This test was carried out outside the SEM under ambient conditions. Of course, the exposure to air humidity could change the properties of the electrolyte, as it is not stable under ambient atmosphere in the long term; however, it should not significantly affect the conditions of the test, as

---

[4]1-Ethyl-3-methylimidazolium tetrafluoroborate

the mechanical properties of the liquid are of interest. Unfortunately, the measurement turned out to be very unstable. The droplet sometimes changed its shape, for example crawled along the tip, and this effect was accompanied by a sudden change of the probe resonance frequency. Such changes often accompanied probe's approach to the sample as the movement of the LiteScope macromotors occurs abruptly. This change in resonance frequency, which affects the feedback, resulted in the probe "crashing" into the sample, suffering mechanical damage. Although scanning with such a tip was still possible, the resulting scan had poor resolution (see Figure 3.5c,d). Stable imaging conditions were achieved only in a single instance (see Figure 3.5e,f).

Next, I created a working cell similar to that in [26] by assembling a cell with a highly oriented pyrolytic graphite (HOPG) as a negative electrode and an NMC-covered aluminium foil as a positive electrode. The HOPG crystal was exfoliated at least 15 times before the measurement (as per the supplementary information of [26]). The working electrode of the potentiostat (EmStat4S) was connected to the HOPG crystal, while the NMC was connected to both the counter and reference electrodes of the same potentiostat. This assembly would then be covered by the electrolyte. Because this sample cannot be transferred without exposure to air (electrical connections are an issue for all available clean sample transfer systems), the electrolyte was added to the sample as the last step just before the chamber of the SEM was evacuated. Scanning the HOPG surface while the battery is being cycled should in theory reveal the process of the SEI formation. However, before the battery was cycled, I intended to perform a scan of the pristine HOPG surface after the application of the electrolyte. Unfortunately, the system turned out to be even more unstable than under ambient conditions. The resonance frequency of the probe was rapidly changing even though the electrodes were not connected to the potentiostat. The most successful scan on a pristine HOPG surface in the electrolyte is shown in Figure 3.6. I did not succeed with the scan on a charging battery.

Although the measurements presented in this section were largely unsuccessful, they have revealed that fluid AFM is indeed possible with LiteScope. If a workflow that prevents the tip from crashing into the sample is developed in the future, it might open the door for further use-cases of LiteScope outside the SEM. Some biological samples (e.g. erythrocytes in blood) are not transparent and could benefit from the possibility of being imaged with a self-sensing probe, such as Akiyama. The problem with turbid liquids is that standard AFM microscopes rely on optical detection of the cantilever deflection, which is not possible if light is dispersed in the environment of the sample. Self-sensing probes are therefore the tool of choice for such samples [28].

3.7 Lithium transport in a solid state electrolyte

In Section 3.5, the potential of SSBs was discussed. In this section, I present a case study in which the C-AFM is utilised to probe the properties of an SSE. The tip is used as an electrode to perform local electrodeposition of lithium, while the process is simultaneously observed with the SEM. The experiment utilises the LiteScope microscope performing an IV spectroscopy on a half-cell which acts as a sample. A half-cell is an electrochemical cell (a battery) with one of the electrodes missing. A cathode-free SSB half-cell is depicted in Figure 3.7. The crucial benefit of the SEM is the possibility to simultaneously measure
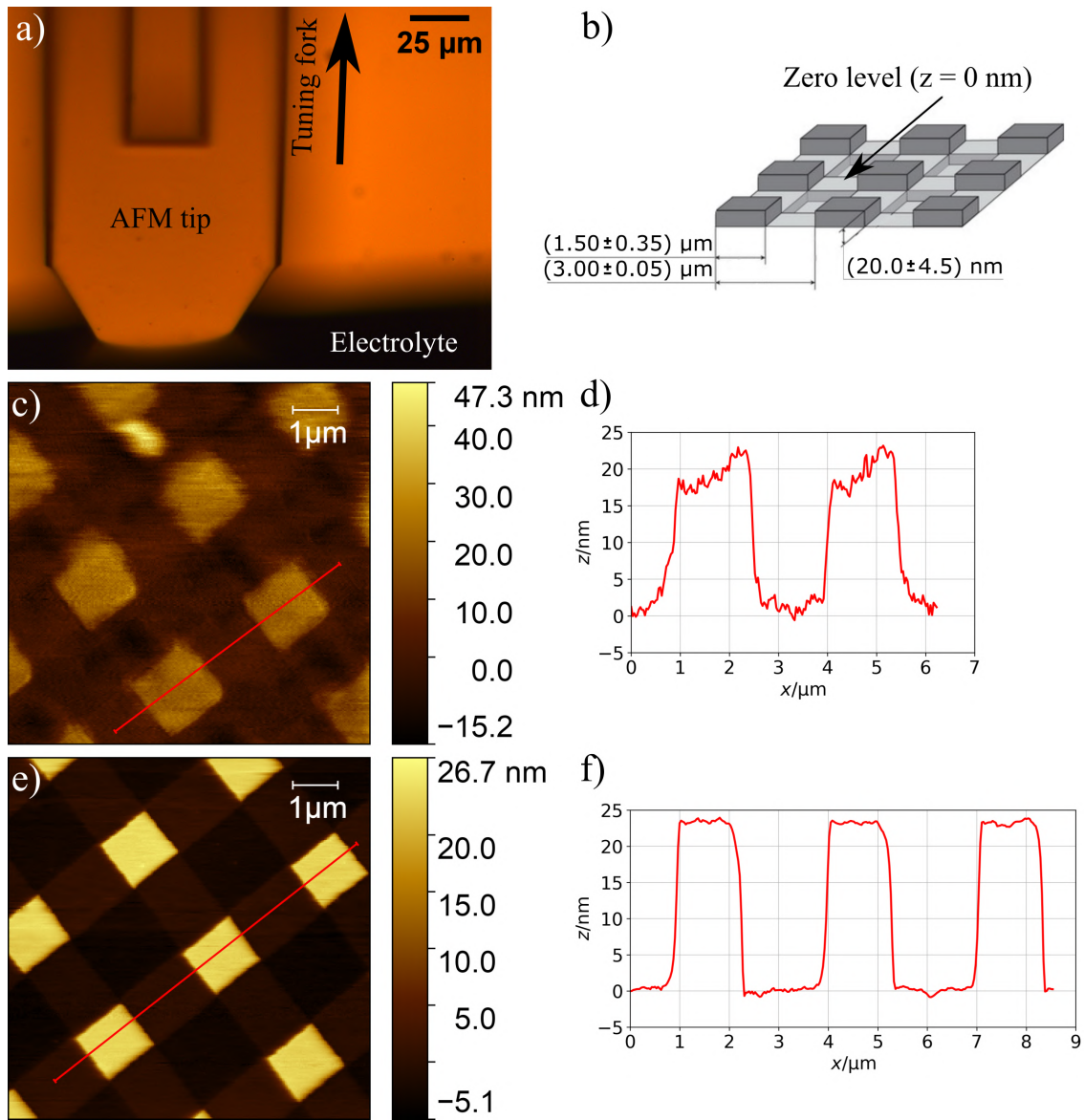
Figure 3.5: The measurement of an AFM test grid submerged in liquid electrolyte. **(a)** An optical image (top view) of the AFM probe in the electrolyte. **(b)** A schematic image of the TGQ1 grid showing its dimensions. **(c)** A typical Fluid AFM measurement of the grid inside the electrolyte (*z*-axis is shifted accordingly to the panel (b)) and **(d)** a line profile extracted along the red line in the panel (c). **(e)** A rare stable Fluid AFM measurement of the grid inside the electrolyte (*z*-axis is shifted accordingly to the panel (b)) and **(f)** a line profile extracted along the red line in the panel (e). Panel (b) adapted from [27].

the current flowing through the cell and to observe the lithium depositing underneath the probe. This experiment is inspired by [29] and particularly [30], where they use an SEM microprobe instead of an AFM probe to deposit a lithium "whisker" which they utilise further for the investigation of lithium intercalations. As microprobes do not have a vertical position feedback (they do not lift from the surface when Li deposits), they create small lithium whiskers instead of the pillars that we grew. I performed the experiments presented in this section in collaboration with my colleague, Bc. Jan Kramář, who also arranged for the sample to be provided by the BELLA laboratory, which is a joint venture
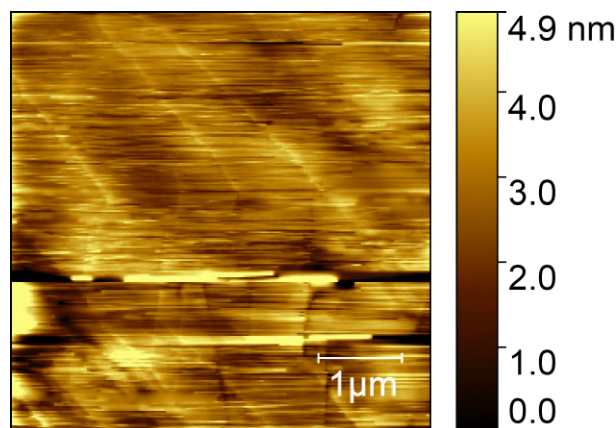
Figure 3.6: A Fluid AFM scan on a pristine HOPG surface inside liquid electrolyte.

between the Karlsruhe Institute of Technology and the BASF company. All experiments in this section have been performed using the NPC probes.
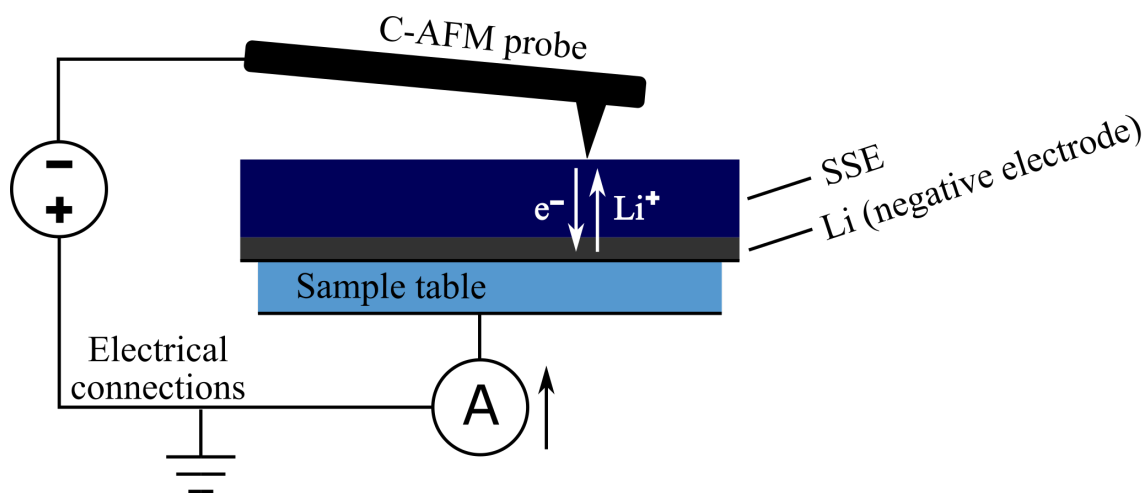

Figure 3.7: A cathode-free SSB half-cell with a conductive AFM probe on top (side view, projection to a plane parallel to the probe cantilever). The probe has a negative bias and therefore Li^+ ions are driven through the SSE from the negative electrode (anode) to the AFM probe. Electrons flow in the opposite direction but the electronic conductivity of the SSE should be negligible compared to its ionic conductivity (unless a metallic connection, i.e. a dendrite, forms between the probe and the negative electrode).

The setup of the experiment is shown in Figure 3.8. The sample consists of a thick (~1 mm) layer of SSE (Li_6PS_5C) and two thinner (~100 µm) metal foils made of indium and lithium. Lithium functions as the active material of the SSB while indium is added to form InLi with lithium through the solid state diffusion. An InLi negative electrode provides significantly enhanced interfacial stability with the SSE compared to electrodes made solely of lithium [31]. The fundamental operation principle remains unchanged from a cell that does not include indium. Both lithium and the SSE are air-sensitive and can only be exposed to an inert atmosphere. As lithium reacts even with nitrogen, argon is the atmosphere of choice. The sample is stored in an argon-filled glovebox between the experiments. The transfer between the glovebox and the SEM is facilitated via a system called *CleanConnect* [32]. The CleanConnect sample transfer system is based on a small sample capsule which can be connected to the SEM load-lock system and to a port on the

glovebox. The sample inside the capsule is attached to a *sample shuttle* which is mounted to the end of a transfer rod. When the CleanConnect is connected to the SEM load-lock, the capsule is pumped, shutters are opened and the transfer rod can be used to insert the sample into the chamber. A CleanConnect attached to an SEM is shown in Figure 3.9a. The LiteScope microscope used in this kind of experiments needs to be equipped with a special stage compatible with the CleanConnect sample transfer system (see Figure 3.9b).
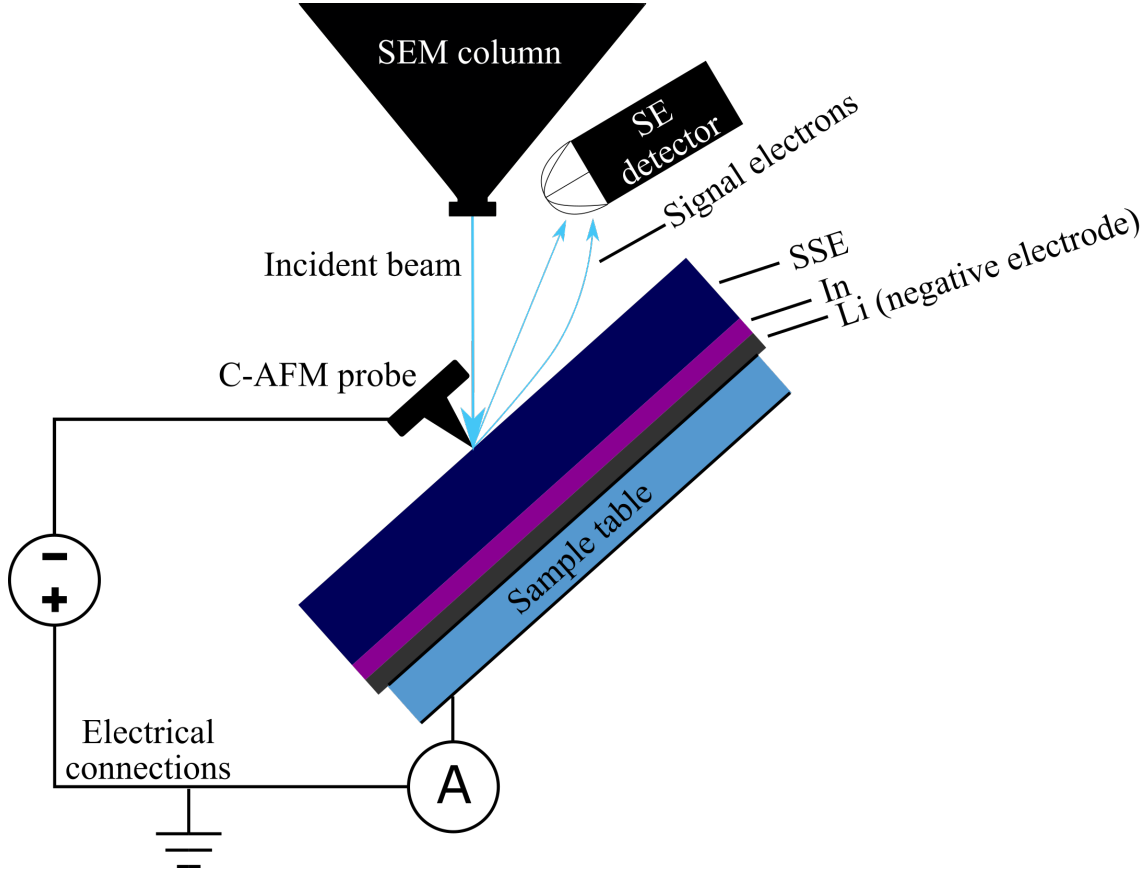

Figure 3.8: The experimental setup used for probing the properties of the SSE (front view, projection to a plane perpendicular to the probe cantilever). LiteScope is tilted to enable the SEM beam to observe the tip of the C-AFM probe. The probe is positioned on top of a half-cell composed of In and Li foils and an SSE layer.

An IV spectroscopy (a "sweep") of the tip bias is performed during the experiment with the sample being grounded. The sweep starts with a positive bias V_{sweep} being applied to the probe. The bias then decreases linearly with time until the voltage $-V_{sweep}$ is reached. At this point, the process repeats starting at $-V_{sweep}$ with the bias increasing to the point where the tip voltage is once again equal to V_{sweep}. LiteScope is limited to $V_{sweep} \leq 10\,V$, however, such high value results in the ammeter under the sample (see Figure 3.7) being saturated at current higher than $51.7\,nA$ anyway and, except for initial attempts, we mostly limited ourselves to narrower ranges.

It is important to note that the incident electron beam of the SEM (the *e-beam*) does not significantly influence the results of the IV sweep. The current of the e-beam that we used is not large enough to significantly influence the result of the measurement. It only creates an insignificant background. The result of a $4.2\,V$ to $-4.2\,V$ sweep performed while the probe was not in conductive contact with the sample is shown in Figure 3.10. In the
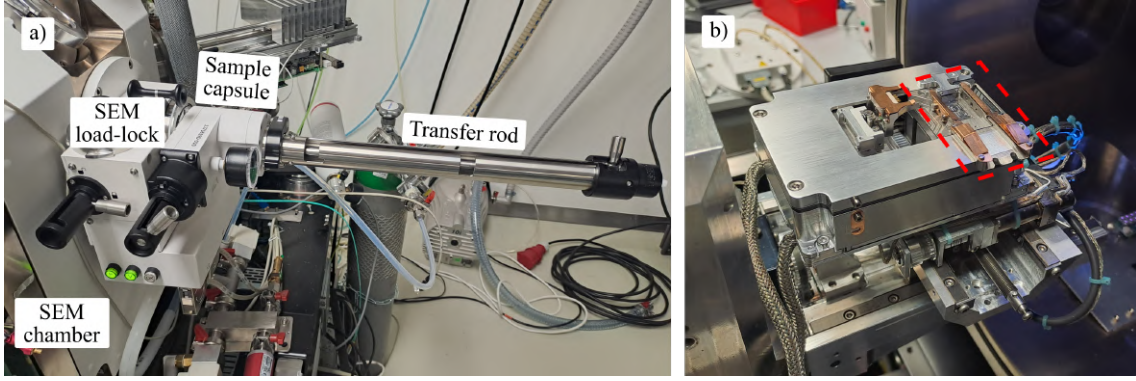
Figure 3.9: The components of the sample transfer system. (**a**) The CleanConnect sample transfer system mounted to the Quattro SEM. The sample inside the sample capsule has not been exposed to air during transfer from the storage glovebox to the SEM as it was either under an inert atmosphere or under vacuum for the whole time. (**b**) A LiteScope with the CleanConnect-compatible stage. The customized part is highlighted by a red parallelogram.

experiment, the e-beam current was 28 pA which was a typical value for our experiments, although on one occasion we used current as large as 110 pA due to an alignment issue of the SEM.
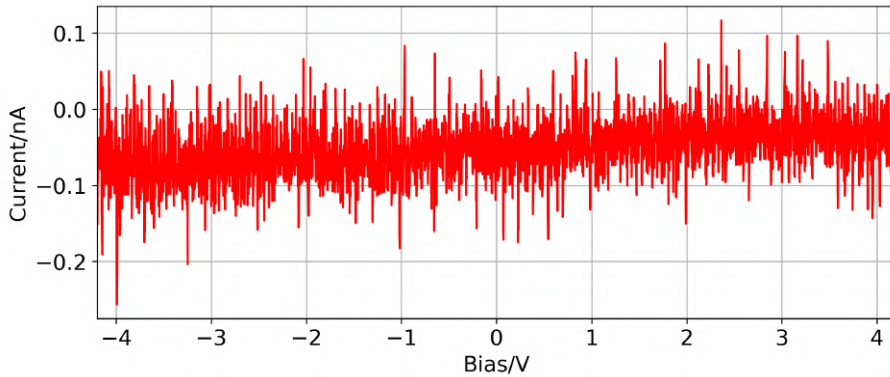

Figure 3.10: An IV sweep performed while the probe and the sample were illuminated by the e-beam and were not in conductive contact. The current of the e-beam was 28 pA. The LiteScope ammeter measures the current through the sample (a so-called *measuring sample configuration*).

During our initial attempts, we discovered that the observed result is heavily dependent on the quality of the conductive contact between the tip and the sample. Sometimes, when the tip is contaminated, no current, except for the current induced by the e-beam, was detected by the ammeter. On other occasions, the pillar starts growing, but after some time, the conductive contact is lost, the current immediately drops to 0 nA and no changes occur afterwards. A fine example of this effect is one of our initial attempts, which is depicted in Figure 3.11. It was the first time we observed a successful controlled electrodeposition. The IV sweep was set to the widest possible range of $V_{bias} = 10$ V. Unlike the microprobes used in [30], the AFM probe in LiteScope has vertical position feedback that maintains a constant force between the probe and the sample. Therefore, when lithium starts depositing underneath the tip, the sample starts moving down (LiteScope is a scanning-sample SPM, the tip remains stationary), and a pillar instead of

a whisker is deposited. In the experiment, a quick deposition of lithium took place when the tip reached negative bias. However, the majority of lithium did not move back to the negative electrode when the tip bias reached positive values again. We speculate that the quality of conductive contact between the pillar and the sample is the reason for the unstable behaviour. The width of the sweep also caused a very large amount of lithium to deposit. The large mass makes the experiment difficult to evaluate or to control precisely.
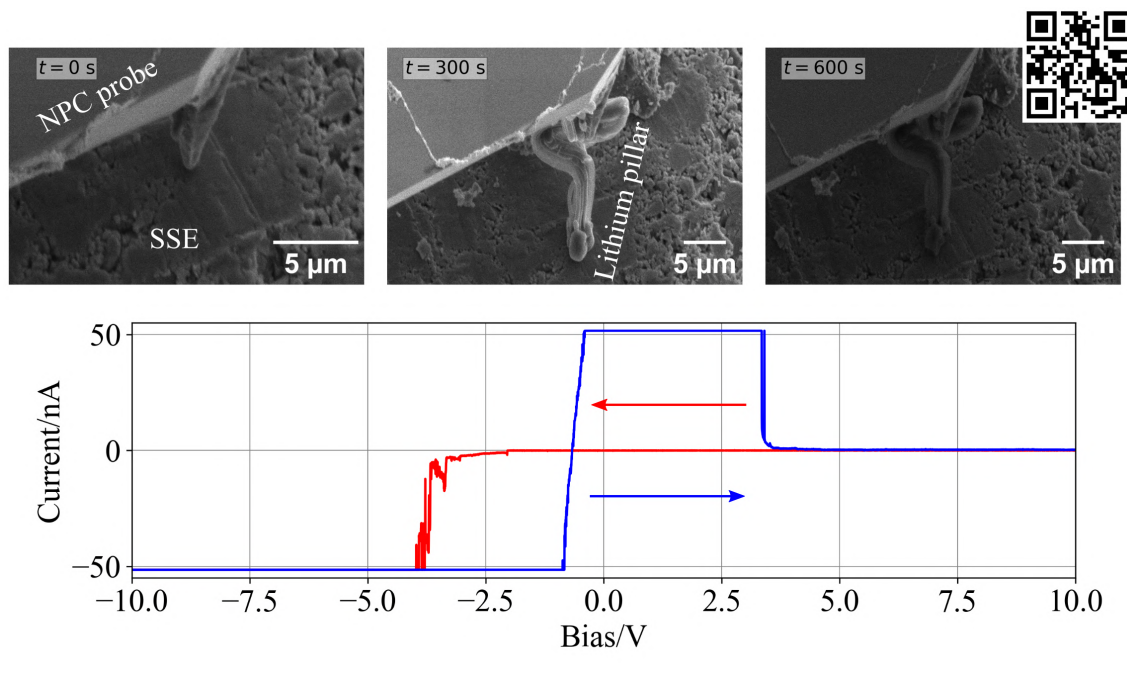

Figure 3.11: The first successful electrodeposition of a lithium pillar on a half-cell. A wide IV sweep ($V_{sweep} = 10\,\mathrm{V}$) was performed. The initial state is shown in the top left image, the state after the first half of the sweep (from $4.4\,\mathrm{V}$ to $-4.4\,\mathrm{V}$) is shown in the top middle image and the final state is shown in the top right image. The red curves show data from the first half of the sweep, and the blue curves show data from the second half. Low magnitude current ($-1\,\mathrm{nA}$) started flowing through the half-cell at the bias $-2.0\,\mathrm{V}$ with a narrow pillar (diameter ~$400\,\mathrm{nm}$) starting to grow. The growth quickly accelerated until at around $-4\,\mathrm{V}$ the ammeter saturated at the bottom of its range ($-51.7\,\mathrm{nA}$). The growth continued and a thick pillar eventually deposited underneath the tip. Although the direction of the current reversed during the second half of the sweep at voltage slightly lower than $0\,\mathrm{V}$, the pillar did not shrink significantly, only its lower part became thinner. The current then abruptly dropped to $0\,\mathrm{nA}$ at around $3.5\,\mathrm{V}$, presumably because a loss of conductive contact between the pillar and the sample or between the probe and the pillar. Notice the variation in magnification across the images, necessitated by the desire to capture the entire development of the pillar. The images were taken by an SEM in SE detection mode at $5\,\mathrm{kV}$. The contrast change results from the change in probe bias influencing the SEs, as they are emitted from the sample with energies below $50\,\mathrm{eV}$ and are therefore sensitive even to the low voltage used to bias the probe. A video of the experiment is available through the QR code in the Figure or at: `https://youtu.be/wlrncVutpL0`

In the following experiments, we used narrower IV sweeps, always with $V_{sweep} < 5\,\mathrm{V}$. We also recorded more signals detected by the SPM. In addition to the current through

Start of electrodeposition						
$-1.2\,\mathrm{V}$	$-1.2\,\mathrm{V}$	$-2.0\,\mathrm{V}$	$-3.1\,\mathrm{V}$	$-3.5\,\mathrm{V}$	$-3.7\,\mathrm{V}$	$-3.8\,\mathrm{V}$

Table 3.2: Voltages at which electrodeposition was initiated, from highest to lowest. The electrodeposition was always initiated in the first half of the IV sweep, while the bias was still decreasing.

the sample, we captured the information about probe deflection which is called *process value.* LiteScope uses its vertical position (z-coordinate) feedback to maintain the process value constant at the setpoint value. If the deflection and consequently the process value increase (e.g. because the pillar starts growing underneath the tip and pushes against it), the sample is moved down to maintain a constant setpoint. A constant setpoint means that the probe-sample interaction is also constant, which is desirable. The default setpoint value for NPC probes in LiteScope in contact mode is $10\,\mathrm{mV}$. Another signal that we detected was the z-coordinate of the piezo controlled sample table. The size of the deposited pillar can be determined from this signal. It is important to note that this signal is subject to thermal drift caused by the thermal expansion of the piezo. As the drift is approximately linear, we can perform a correction by subtracting a linear function fitted to the part of the z vs. bias curve, where no lithium is deposited (i.e. nothing is happening), usually during the start of the spectroscopy. However, this approximation is far from perfect, as the drift usually slows down over time.

The experiments start with a period during which nothing is happening, as the voltage decreases from V_{sweep} to a negative voltage at which the electrodeposition is initiated. Surprisingly, this value is not always the same. In our experiments, we observed the lithium pillars to start growing between $-1.2\,\mathrm{V}$ and $-3.8\,\mathrm{V}$ (see Table 3.7). As the bias once again rises above the voltage that initially triggered the electrodeposition, the pillar begins to shrink, even though the bias remains negative. A representative case of such behaviour is shown in Figure 3.12. The shrinkage of the pillar is accompanied by current flowing in the opposite direction (i.e. from the probe to the sample). However, the majority of lithium often remains in the pillar because the flow of current either ceases completely as in Figures 3.11 and 3.12 or the current drops to a very low value (presumably due to loss of contact). After several attempts, we identified the conditions necessary to perform a repeatable electrodeposition. First and foremost, we only deposited a small pillar (i.e. we used a narrow sweep). Secondly, we increased the tip-sample force by using a setpoint larger than usual. With these conditions, we were able to perform a deposition of a small pillar which was subsequently embedded back to the half-cell. This experiment is shown in Figure 3.13.

These experiments demonstrate a possible use-case for LiteScope as a tool for probing the conductive properties of SSEs. Such experiments can be used to study the characteristics of composite SSEs, potentially revealing variations in conductivity among the individual phases. Interestingly, we discovered that the bias that initiates electrodeposition is not always the same. We speculate that this effect could be caused by local inhomogeneities in the SSE or it could be one of the effects of poor conductive contact between the probe and the SSE. It is possible that one of the influences on the cell voltage mentioned in Section 3.2 influences the voltage. A more thorough investigation would also require us to utilise cyclic voltammetry together with a potentiostat instead of a simple IV sweep. The
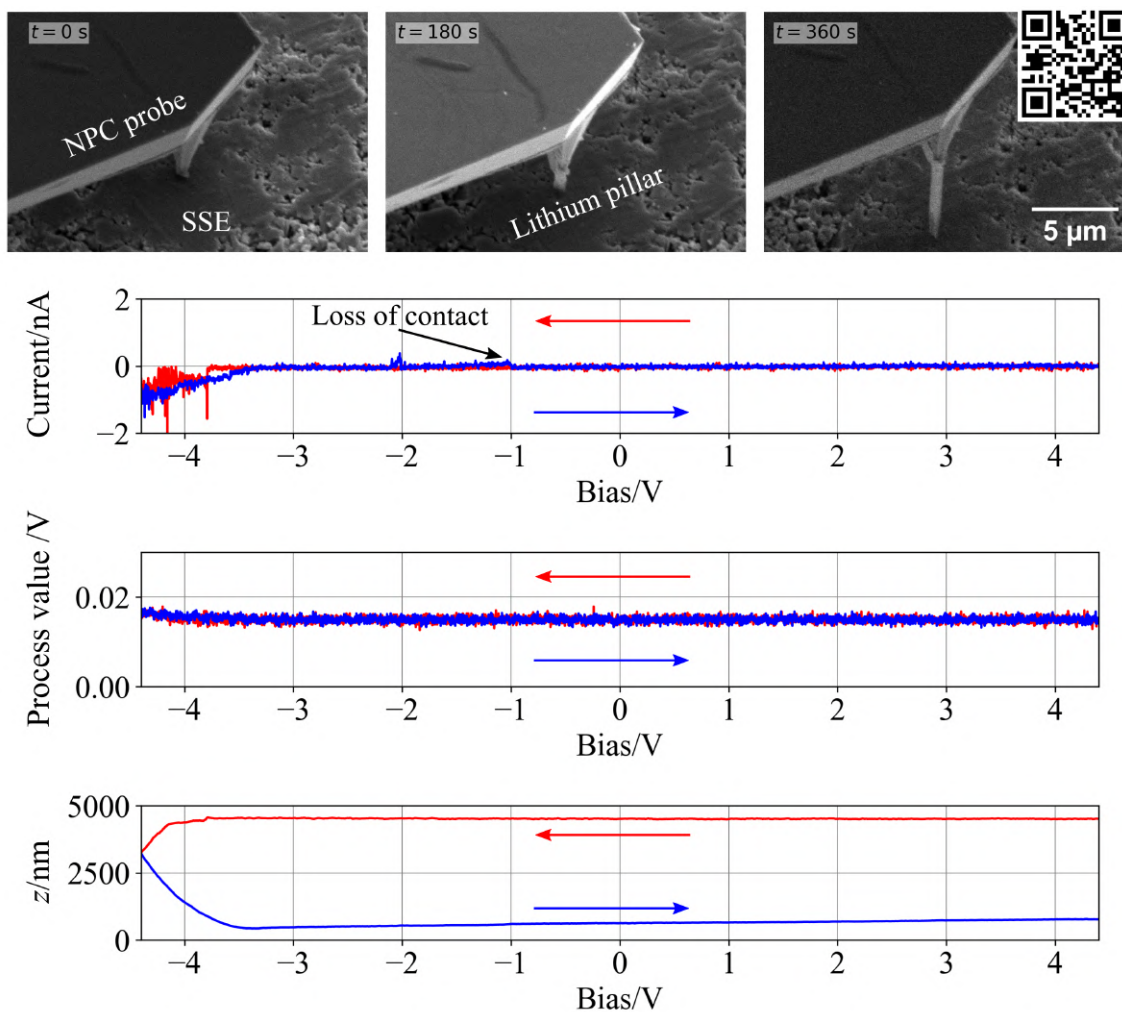
Figure 3.12: A lithium electrodeposition experiment on a half-cell. A narrow IV sweep ($V_{sweep} = 4.4\,\text{V}$) was performed. The initial state is shown in the top left image, the state after the first half of the sweep (from $4.4\,\text{V}$ to $-4.4\,\text{V}$) is shown in the top middle image and the final state is shown in the top right image. The red curves show data from the first half of the sweep, and the blue curves show data from the second half. The current suddenly started flowing through the half cell when the bias $-3.8\,\text{V}$ was first reached and it was accompanied by the deposition of the lithium pillar. The pillar grew until it reached the height of $4\,\mu\text{m}$. When the bias reached $-3.4\,\text{V}$ during the second half of the sweep, the current changed direction and the pillar started to shrink. The shrinkage stopped at $-1\,\text{V}$, at which the current ceased altogether (presumably due to loss of contact). The images were taken by an SEM in SE detection mode at $5\,\text{kV}$. The contrast change results from the change in probe bias influencing the SEs, as they are emitted from the sample with energies below $50\,\text{eV}$ and are therefore sensitive even to the low voltage used to bias the probe. A correction has been applied to the z-coordinate to account for the linear drift, determined by a linear fit of the z-coordinate across the bias range from $4.4\,\text{V}$ to $0\,\text{V}$. A video of the experiment is available through the QR code in the Figure or at: https://youtu.be/Lsqg3IWK4tI
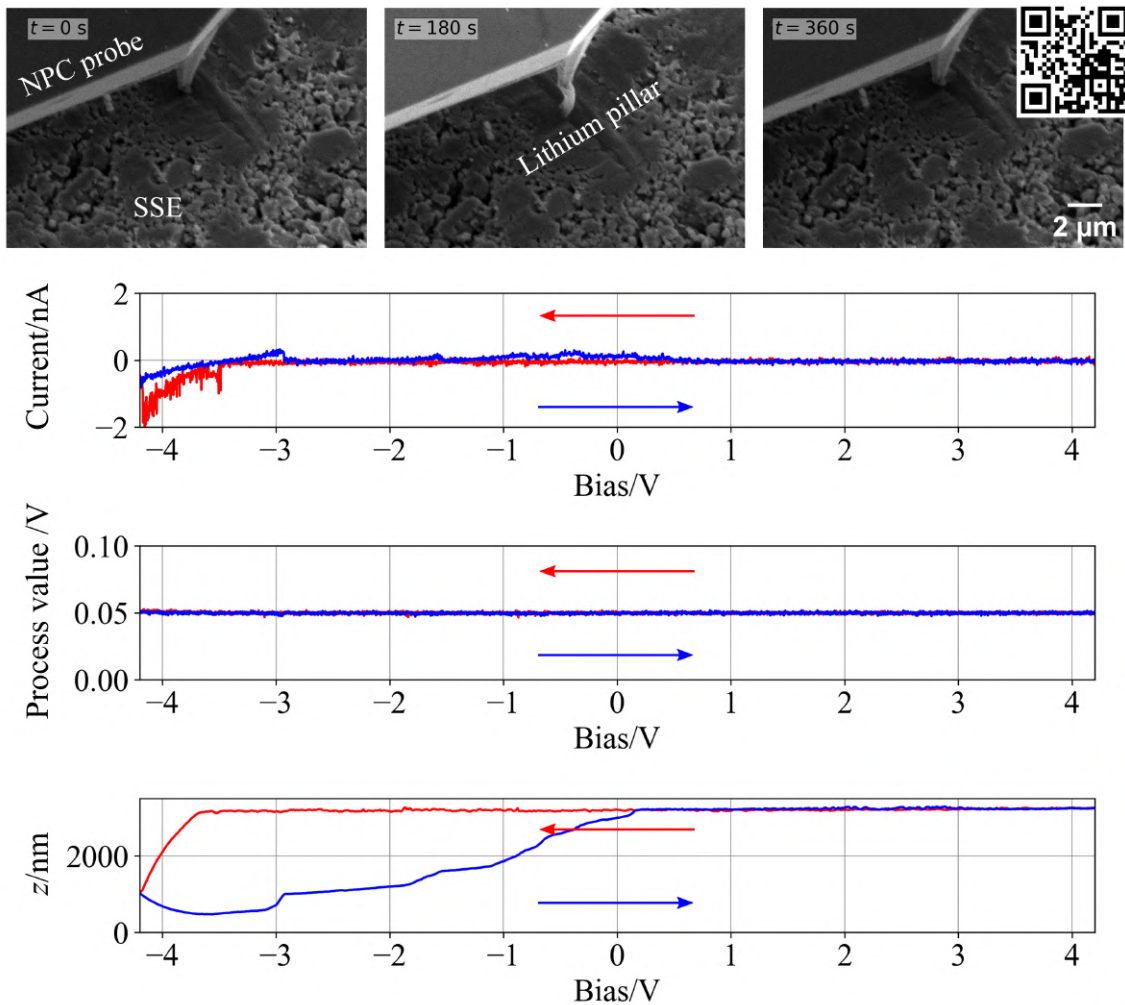
Figure 3.13: A repeatable lithium electrodeposition experiment on a half-cell. A narrow IV sweep ($V_{sweep} = 4.2\,\mathrm{V}$) was performed. The initial state is shown in the top left image, the state after the first half of the sweep (from $4.2\,\mathrm{V}$ to $-4.2\,\mathrm{V}$) is shown in the top middle image and the final state is shown in the top right image. The red curves show data from the first half of the sweep, and the blue curves show data from the second half. A setpoint increased to $50\,\mathrm{mV}$ was employed, in contrast to the lower values used in previous measurements. Current started flowing through the half-cell at bias $-3.5\,\mathrm{V}$ and this was accompanied by the deposition of the lithium pillar. In contrast to the other experiments, this time the whole pillar was gone at the end of the sweep. This is apparent from the SEM image as well as the z-coordinate plot. The images were taken by an SEM in SE detection mode at $5\,\mathrm{kV}$. The contrast change results from the change in probe bias influencing the SEs, as they are emitted from the sample with energies below $50\,\mathrm{eV}$ and are therefore sensitive even to the low voltage used to bias the probe. A correction has been applied to the z-coordinate to account for the linear drift, determined by a linear fit of the z-coordinate across the bias range from $4.2\,\mathrm{V}$ to $0\,\mathrm{V}$. A video of the experiment is available through the QR code in the Figure or at: https://youtu.be/4VxE6OkHtuI

26

utilisation of a potentiostat which is equipped with a reference electrode could increase the robustness of our experiments.

One more potential application rests with an article mentioned at the beginning of this section. In [30], the authors investigated the properties of lithium intrusions (i.e. dendrites) in an SSE and the effects of microstructural defects, which they analysed using a SEM-FIB microscope. In particular, they were interested in the influence that mechanical stress has on the evolution of these intrusions. They applied mechanical force on the sample with a microprobe and then calculated von Mises stress in the SSE using the finite element method. This approach has several drawbacks. Firstly, the apex of the microprobe was simulated as a tungsten sphere with the diameter of 7 μm. However, this is a severe approximation as the apex of the microprobe is of an irregular shape. In contrast, the tip of an AFM probe is much better defined. Secondly, a microprobe lacks the ability to apply mechanical force with the same precision as an AFM tip. Both of these advantages of AFM could potentially benefit a similar experiment in the future.

3.8 MXenes as electrode particles

The use-case demonstrated in the previous section has pointed us to the idea of performing a similar experiment to investigate the properties of positive electrode materials. The half-cell introduced in the previous section is essentially a Li-metal battery (refer to Section 3.4) without a positive electrode. If we could add a material that functions as a positive electrode, we could study a whole battery cell in our microscope. In our experiment, we used a material from the class of 2D materials called *MXenes*. MXenes are a class of materials which are usually produced by etching their parent MAX phase precursor (although synthesis by chemical vapour deposition has also been demonstrated [34]). MAX phases (e.g. Ti_2AlC) consist of early transition metal(s) (M), group A element(s) (A), which usually come from groups 13 – 15 in the periodic table, and nitrogen or carbon or their combination (X). The elements forming MAX phases are highlighted in the periodic table in Figure 3.14. The chemical formula of MAX is $M_{n+1}AX_n$ with n ranging from 1 to 3. In MAX phases, the elements are stacked in a layered structure. If the A layer is selectively etched (see Figure 3.15) from the MAX phase, a 2D material stack denoted by chemical formula $M_{n+1}X_nT_x$ remains (T is the termination group introduced by the acid, e.g. –OH). This 2D material stack is dubbed MXene. In theory, synthesis of MXenes without the termination group should be possible, but the current approaches to their synthesis have failed to produce them so far [33, 36, 37]. MXenes are conductive and they are considered to be contenders for future applications in batteries in both negative (Li-ion) and positive (Li-metal) electrodes. While the applications in the negative electrodes of metal-ion batteries (especially Li-ion batteries) have garnered significant attention [38], the employment of MXenes in positive electrodes of batteries with pure-metal-based negative electrodes (i.e. Li-metal, Mg-metal, etc.) are also emerging. For example, in Li-sulphur batteries MXenes can be employed to stabilise the positive electrode and prolong its lifetime [39]. MXenes themselves are also investigated for being a prospective material for positive electrodes. In [40], they were employed in a hybrid magnesium/lithium-metal battery as a positive electrode material. Here, we have attempted to construct a similar Li-metal SSB with an MXene-based positive electrode.

Figure 3.14: The elements which have been observed to form a MAX phase (as of 2017) coloured by their role in the MAX phase. Reproduced from [33].
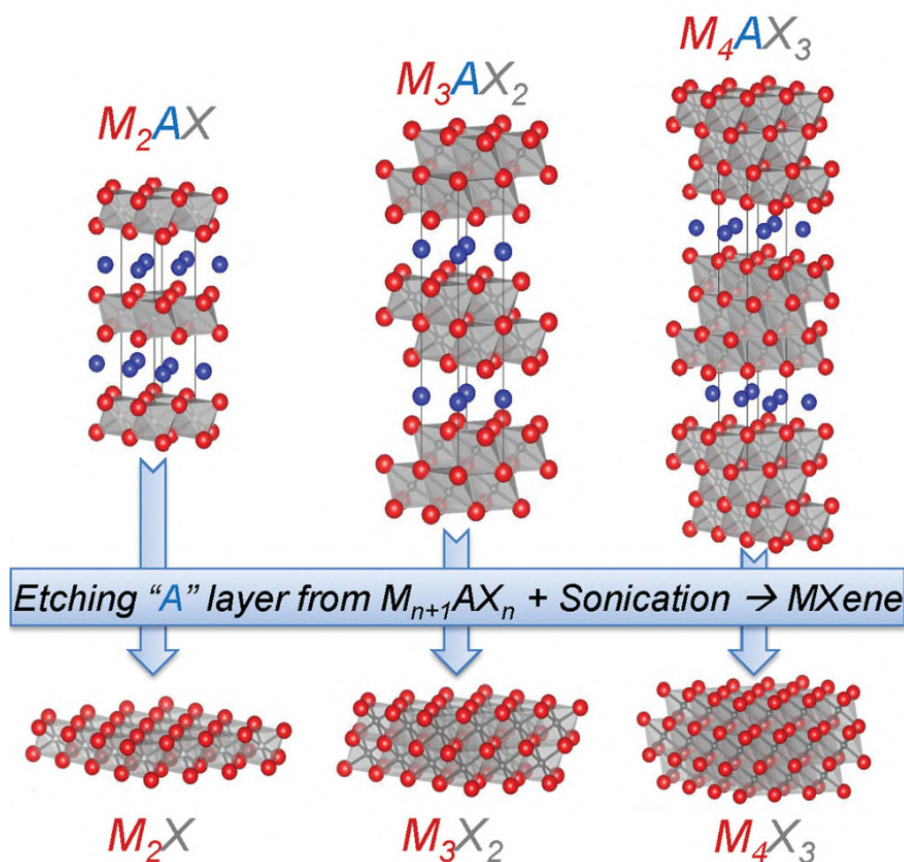

Figure 3.15: The synthesis of MXenes (2D) from MAX phases (3D) with $n = 1$ (left), $n = 2$ (middle), and $n = 3$ (right). The A compound in the original MAX phase is selectively etched away and the resulting structure is split into individual layers by sonication. Reproduced from [35]

In the experiment, we used the sample introduced in the previous section (the half-cell) with MXene particles drop-casted on top of it. These particles (see Figure 3.16) have been provided by Dr. Minghao Yu (Technical University Dresden). In contrast to a real battery, these particles had worse contact to the electrolyte as an SSB positive electrode usually consists of active material particles (e.g. NCA or NMC) dispersed in a matrix made of an SSE. An example of a cross-section through an SSB positive electrode is shown in Figure 3.17. The particles in our sample have only been placed on top of the
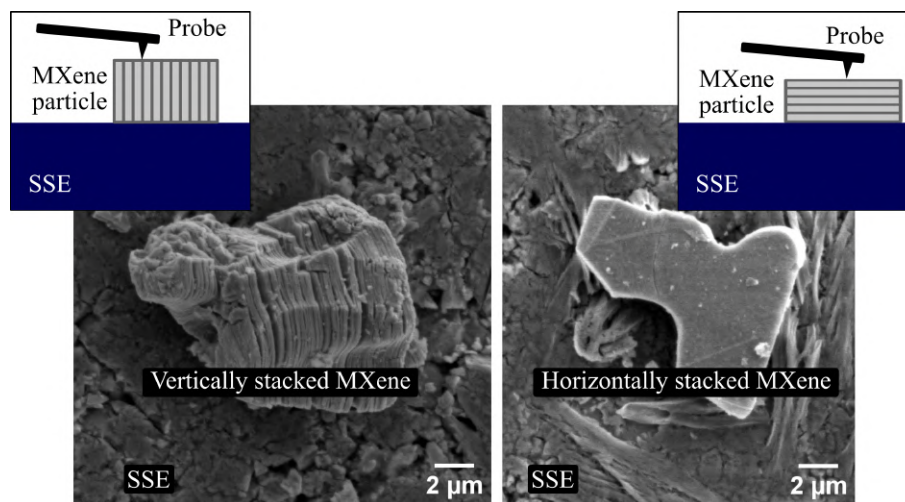
28

Figure 3.16: Two possible orientations of drop-casted MXene particles ($Ti_2C_{1/2}N_{1/2}BO_2$) on top of the SSE (Li_6PS_5C). The layers of the particle on the left are arranged perpendicular to the substrate, whereas those of the particle on the right are parallel to the substrate. Insets depict side views where AFM probes are positioned on top of the particles. Sample courtesy of Minghao Yu.
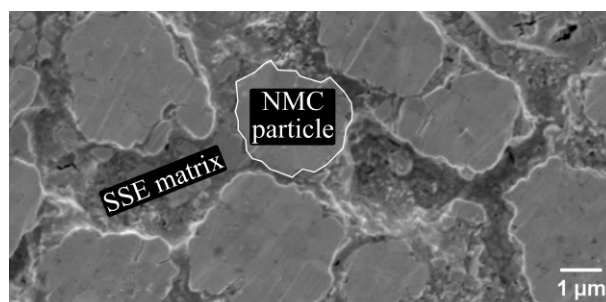

Figure 3.17: A cross-section through a positive electrode of an SSB. Several NMC particles are embedded in a matrix made of an SSE. Image has been taken by an SEM at $2\,kV$ in SE detection mode. Sample courtesy of BELLA laboratory and NenoVision.

SSE instead of being embedded in it. Our initial idea was to perform the same IV sweep as in the previous section with the tip located on top of an MXene particle. The Li^+ ions would migrate from the negative electrode toward the MXene particle, which would serve as a positive electrode, and integrate into it. The same process takes place during the discharging of an actual battery.

Our initial assumption had been that we could observe the volume of the particles to change during (dis)charging by capturing the z-coordinate development during the IV sweep or by observing it with the SEM. We had also aimed to investigate possible differences between horizontally and vertically stacked MXenes (see Figure 3.16). However, the real system proved to be more complex. In one measurement on a vertically stacked particle (see Figure 3.18), we saw dramatic expansion taking place in the z-coordinate. In an ordinary AFM (i.e. outside the SEM), we could assume that the particle is growing during the sweep, just as we assumed. However, a thorough investigation of the SEM images reveals that the particle did not undergo any observable changes and the growth was instead caused by "swelling" of the SSE under the particle. All of these observations raise an important question that we were unable to answer. Do Li^+ ions really embed

inside the MXene particles or do they only deposit themselves underneath the particles? Since Mxenes are conductive, they could act as current collectors and we would effectively be performing the experiments from the previous section again, this time with a much larger tip. It is also possible that both of these effects are taking place. Further research is necessary to answer this question. The challenge lies in the fact that standard analytical methods often have a reduced sensitivity to light elements. For example, energy dispersive spectroscopy struggles to detect lithium.

A representative measurement on a horizontally stacked MXene particle is shown in Figure 3.19. This measurement is also supplemented by a second IV sweep performed subsequently on the same particle (see Figure 3.20). This sweep differs from the first one, as it shows positive current flowing in the initial stage of the sweep as well. This behaviour is expected because, at the start of the first sweep, no lithium was present in the particle (or underneath it), while at the start of the second sweep, the particle should already contain lithium from the first attempt (or at least have lithium accumulated underneath it). Two more measurements (one for each orientation) are presented in Supplement A.

In all measurements, we observed an instability in the SEM images when current was flowing through the sample. The SEM images appeared to "shake", suddenly and unexpectedly shifting by hundreds of nanometres, often several times per second. Since no sudden changes were correlated with these shifts in the z-coordinate plot or the process value plot, we assume that the shift happened to the e-beam. It could possibly be caused by changes in the electromagnetic field around the sample associated with the migration of Li^+ ions.
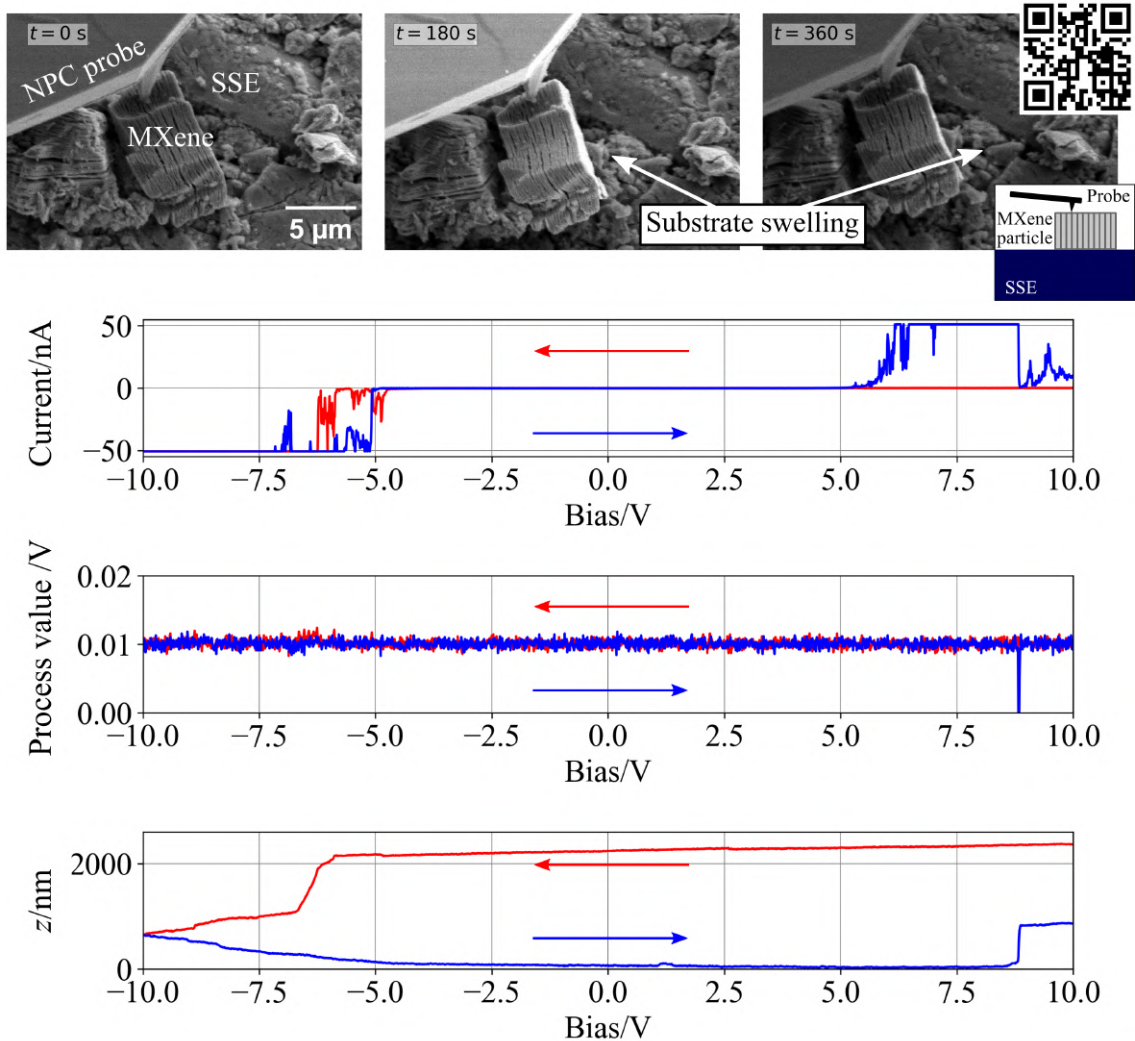
Figure 3.18: Charging of a vertically stacked MXene particle (see inset on the right). A wide IV sweep ($V_{sweep} = 10\,\text{V}$) was performed. The initial state is shown in the top left image, the state after the first half of the sweep (from $10\,\text{V}$ to $-10\,\text{V}$) is shown in the top middle image and the final state is shown in the top right image. The red curves show data from the first half of the sweep, and the blue curves show data from the second half. Although there is no visible change to the MXene particle, the substrate expands during the sweep. No correction has been applied to the z-coordinate to account for the drift. The images were taken by an SEM in SE detection mode at $5\,\text{kV}$. The contrast change results from the change in probe bias influencing the SEs, as they are emitted from the sample with energies below $50\,\text{eV}$ and are therefore sensitive even to the low voltage used to bias the probe. A video of the experiment is available through the QR code in the Figure or at: `https://youtu.be/IdVrINdayEo`.
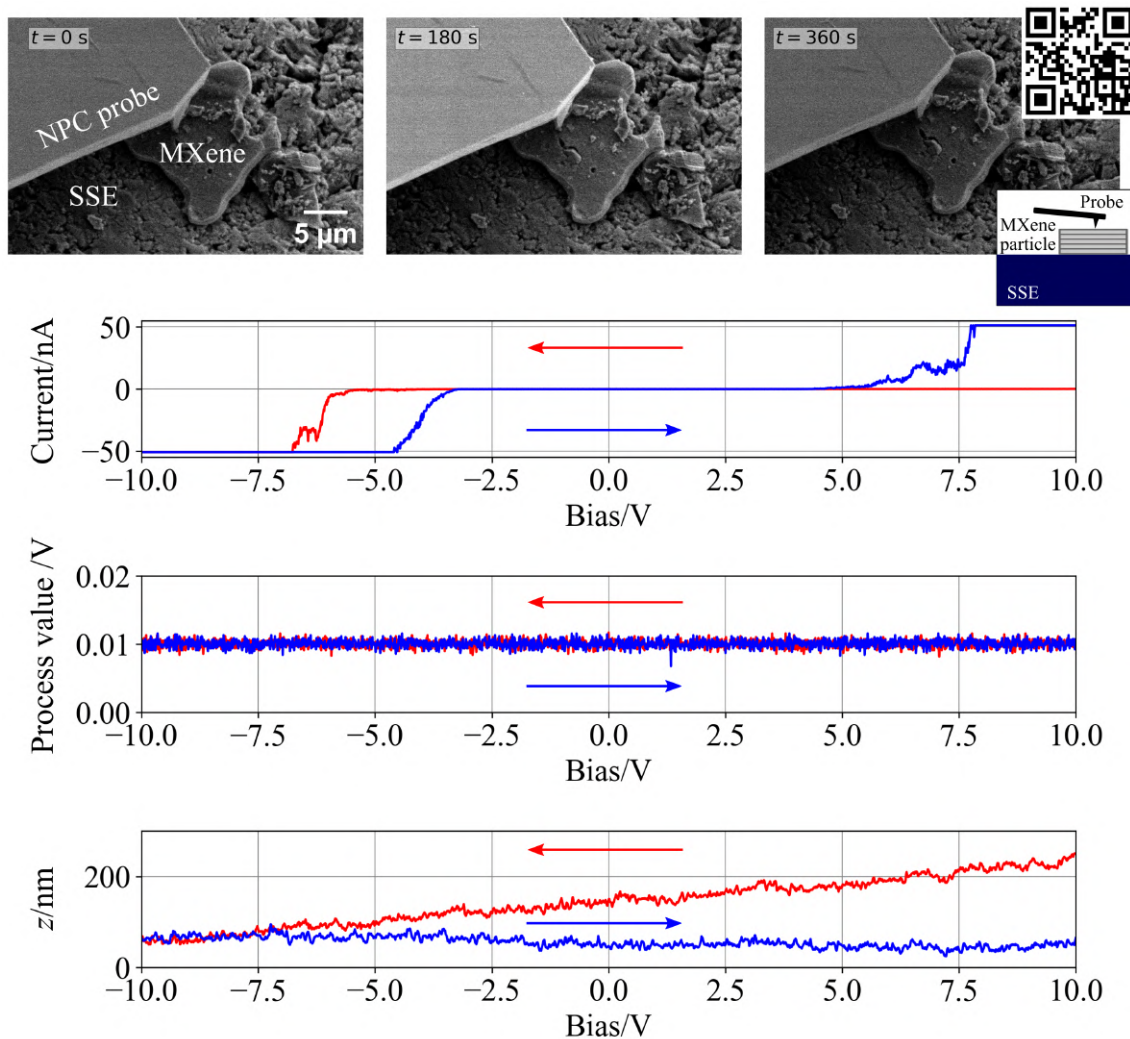
Figure 3.19: Charging of a horizontally stacked MXene particle (see inset on the right). A wide IV sweep ($V_{sweep} = 10\,\text{V}$) was performed. The initial state is shown in the top left image, the state after the first half of the sweep (from $4.4\,\text{V}$ to $-4.4\,\text{V}$) is shown in the top middle image and the final state is shown in the top right image. The red curves show data from the first half of the sweep, and the blue curves show data from the second half. At first, no current flows through the sample at positive bias, however during the second part of the sweep, lithium is driven back to the negative electrode and positive (from the tip to the sample) current is detected. The development in the z-coordinate can be attributed to the scanner drift because the magnitude of current does not affect the z-coordinate. No correction has been applied to the z-coordinate to account for the drift. No visible change was detected by the SEM. The images were taken by an SEM in SE detection mode at $5\,\text{kV}$. The contrast change results from the change in probe bias influencing the SEs, as they are emitted from the sample with energies below $50\,\text{eV}$ and are therefore sensitive even to the low voltage used to bias the probe. A video of the experiment is available through the QR code in the Figure or at: `https://youtu.be/I904tOfFA5c`.
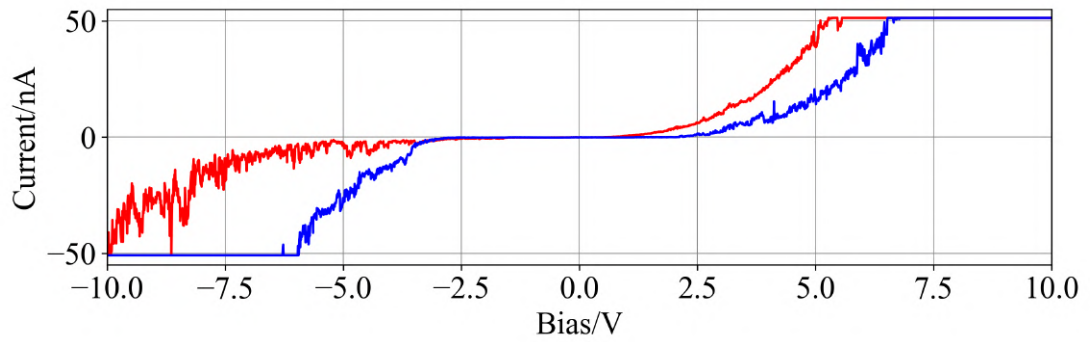
Figure 3.20: A short ($t = 10\,\mathrm{s}$) IV sweep conducted immediately after the measurement shown in Figure 3.19 on the same particle. Unlike during the first sweep, this time, positive current was flowing in the initial stage of the sweep as well. This change in behaviour from the first sweep is expected and can be explained by lithium already being embedded in the MXene particle or deposited under it and consecutively migrating back to the negative electrode.

4 Graphene

Graphene is probably the most well-known two-dimensional material. It consists of carbon atoms arranged in the 2D hexagonal lattice (shown in Figure 4.1a). It is especially interesting because of its electronic properties. Graphene's band structure (see Figure 4.1b) is unusual because its valence and conduction bands touch at the so-called Dirac points. This means that graphene has a zero density of states at the Fermi level but its gap has a zero width. Such materials are called *band-less semiconductors*. This property leads to many interesting effects. For example, suspended graphene has very high electron and hole mobilities at low temperatures (values exceeding $2 \cdot 10^5 \, \mathrm{cm^2 V^{-1} s^{-1}}$ have been reported [43]). Even when it is attached to a surface of, for example, silicon dioxide and under ambient conditions, the mobilities are still on the order of $10^4 \, \mathrm{cm^2 V^{-1} s^{-1}}$ [44]. It is also possible to alter the conductivity type of graphene (switch from p-type to n-type and vice versa) by applying an external electric field and thus create very efficient and fast graphene field effect transistors (GFETs). This so-called Ambipolar electric field effect is shown in Figure 4.1c [44].
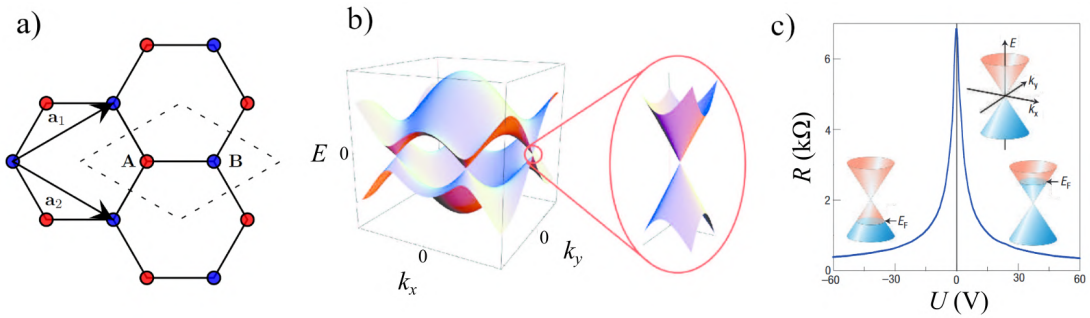

Figure 4.1: **(a)** The graphite (2D hexagonal) lattice. Notice that the unit cell highlighted by a dashed line contains two carbon atoms (marked A and B). Primitive vectors $\mathbf{a_1}$ and $\mathbf{a_2}$ are $2.46 \, \mathrm{\AA}$ long. **(b)** Electronic band structure of graphene. Conduction and valence bands are connected at the Dirac points which are located at the Fermi level ($E = 0$). **(c)** The ambipolar electric field effect (at temperature $T = 1 \, \mathrm{K}$) in a GFET during which the conductivity type and the resistivity R of graphene change based on applied gate voltage V_g. The insets indicate the change in the Fermi level of graphene. Reproduced from [41, 42, 43].

However, achieving the desired electronic properties is only possible under one critical assumption: the graphene must not have any defects in its lattice nor have any contaminants adsorbed to it. In real life, that is difficult to achieve. In this thesis, I am concerned with one specific type of defect, the grain boundary. In order to achieve the desired properties, it is necessary to prepare (exfoliate, deposit, etc.) large graphene single crystals. One method showing promise for facilitating their growth, which is utilised in this thesis, is described in the subsequent section.

4.1 Chemical Vapour Deposition

Chemical vapour deposition (CVD) is a widely used technique for the synthesis of thin layers and coatings. For our purposes, we can take the simplistic approach to CVD and imagine it as a reaction during which gaseous chemicals in the deposition chamber react

on the surface and form layer(s) with the desired composition. More specifically, the precursor molecules (in our case ethylene – C_2H_4) adsorb to the surface and decompose. The dissociation is facilitated by the surface, hence the influence of the surface material on the growth rate. The released carbon atoms then either diffuse along the surface or dissolve in the material and diffuse within it. These atoms then nucleate new crystals or contribute to the growth of preexisting crystals. As these crystals grow, crystal boundaries (i.e. line defects) form at the points of contact. A schematic picture is shown in Figure 4.2 [45].
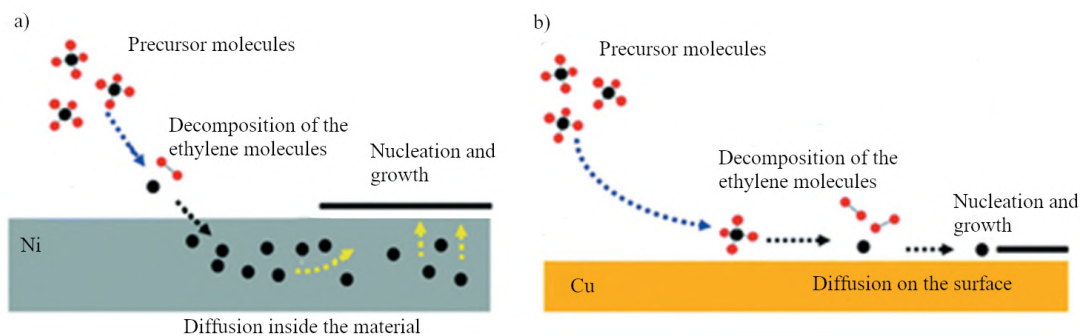

Figure 4.2: A schematic of the graphene growth by CVD. The precursor molecules (C_2H_4) decompose on the surface and release carbon atoms which either diffuse inside the material as is the case with nickel in (**a**) or diffuse along the surface as is the case with copper (**b**). The atoms then create new graphene nuclei or contribute to the growth of preexisting graphene crystals. Adapted from [45].

If we want to grow large graphene crystals to avoid the issues with crystal boundaries (which are illustrated in Figure 4.3a), we have several options. The simplest one would be to grow single large crystals (see Figure 4.3b). In practice, this is difficult to achieve. Another proposed way is to grow graphene epitaxially with the atomic lattice of the substrate (see Figure 4.3c). However, there is another unconventional method. In 2012 it was shown in [46] that graphene can be grown on liquid copper. The graphene crystals were grown floating on a liquid substrate and it was hypothesised that the crystals aligned with each other (self-assembled) as can be seen in Figure 4.4. This effect should help to prevent the formation of grain boundaries (see Figure 4.3d). Upon a thorough examination of Figure 4.4c, it becomes apparent that the vertices of the hexagons are not seamlessly connected to each other. This can be explained by observing the growth of these crystals in real-time. Although the crystals self-align well during the initial stages of growth, they fall out of alignment shortly before connecting together. The understanding of this phenomenon is not yet complete, and it is vital to develop a model of forces acting on and between the graphene crystals. In [47] an interaction model based on capillary forces and electrostatic interaction, as a driving force behind the self-assembly, was suggested. However, the characteristic length (also known as *capillary length*) for such a capillary interaction (for a system on liquid copper) is ~4 mm (from Supplementary Note 6 of [47]). As the capillary force is a result of an interaction between two menisci, the confirmation of this theory requires us to understand the topography of the graphene-on-liquid system. It is crucial to determine whether the crystals are flat, if there is a meniscus at their boundary, and if so, whether it curves above or below the molten metal level.
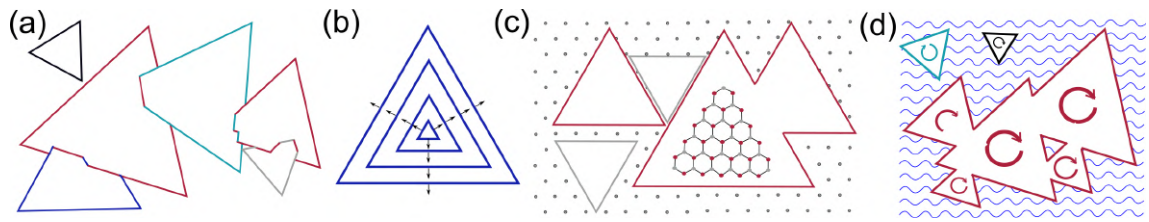
Figure 4.3: Different ways to grow graphene with respect to the occurrence of crystal boundaries. In (**a**) multiple grains grow simultaneously and when they meet each other, their crystal lattices are not mutually aligned. This issue is resolved in (**b**) by growing one single crystal and in (**c**) by growing multiple crystals epitaxially. Another way to avoid crystal boundaries (theoretically) is by growing the graphene on a liquid surface and letting the crystals align with each other (**d**). Image courtesy of Miroslav Kolíbal.
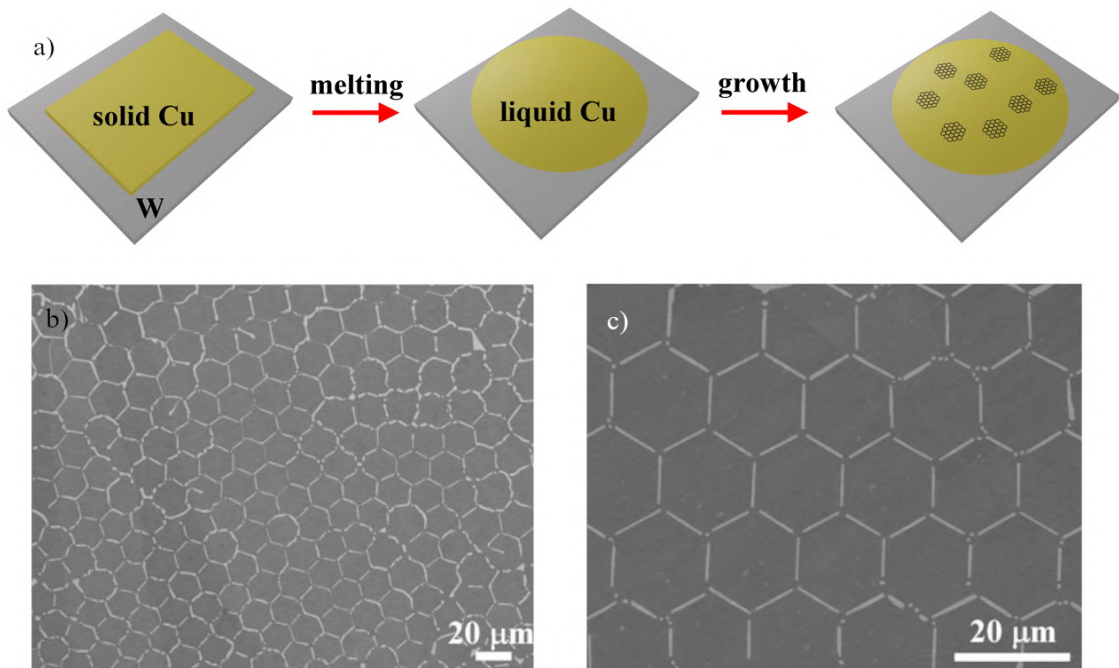

Figure 4.4: Graphene growth on liquid copper. The panel (**a**) schematically shows the experimental workflow. In (**b**) and (**c**) there are hexagonal graphene crystals grown by this method captured by an SEM. The growth had been stopped just before the graphene would cover the entire surface. Reproduced from [46].

4.2 Experimental goals

In this thesis, I aim to expand our understanding of the graphene-on-liquid-metal system. I do so in collaboration with my colleague, Ing. Kristýna Bukvišová, who explores the system as a part of her PhD thesis. Specifically, I will focus on graphene grown on gold because gold is easier to work with (faster sample preparation and much slower evaporation in vacuum compared to copper) and it is potentially a first step toward understanding the same system on liquid copper. Graphene grown on molten metal has so far been mainly studied by optical and electron microscopies [46]. These techniques are invaluable when studying the movement and growth of the crystals in real-time or their morphology. However, neither of them can provide information about the topography of

the sample. If we desire to have a more complete understanding of the sample, we need to employ other techniques, such as the AFM.

The employment of AFM raises several issues. Measurements inside liquids (the fluid AFM) are considered to be relatively routine, with various commercial systems widely available and in common use. That is not the case for measurements on liquid-gas interfaces (surfaces) or for liquids in vacuum. Experimental work has been done in the area of probing liquid-liquid interfaces [48] and imaging molecules trapped inside them [49], but the idea of probing surfaces of liquids remains mostly elusive. However, there are still some cases where this has been accomplished. In 1993, researchers at the Pacific Northwest Laboratory and the University of Utah have published their work on imaging adsorbates on liquid mercury using an STM [50].

My goal is to explore the topography of graphene crystals floating on top of molten gold using the frequency modulated AFM introduced in Subsection 2.1.1. I attempt to answer the questions outlined at the end of Section 4.1.

4.3 Experimental setup

In AFM measurement of graphene on liquid gold, I utilise a setup I developed as a part of my bachelor's thesis [51]. The device allows for sample heating in the LiteScope SPM-in-SEM microscope up to $1\,200\,°C$. This temperature is above the melting point of gold ($1\,063\,°C$ [52]). Heating is carried out by a micro-electromechanical chip µHeater developed by Thermo Fisher Scientific. Figure 4.5 shows a LiteScope with the heater installed. This setup has the advantage of minimal power output. The amount of heat transferred into the AFM is negligible, keeping the piezo positioners (scanners) at their standard temperature and thus minimising the thermal drift of the sample. One drawback of this configuration is the diameter of the heated region of only $100\,\text{um}$, requiring the samples to be of a corresponding size.
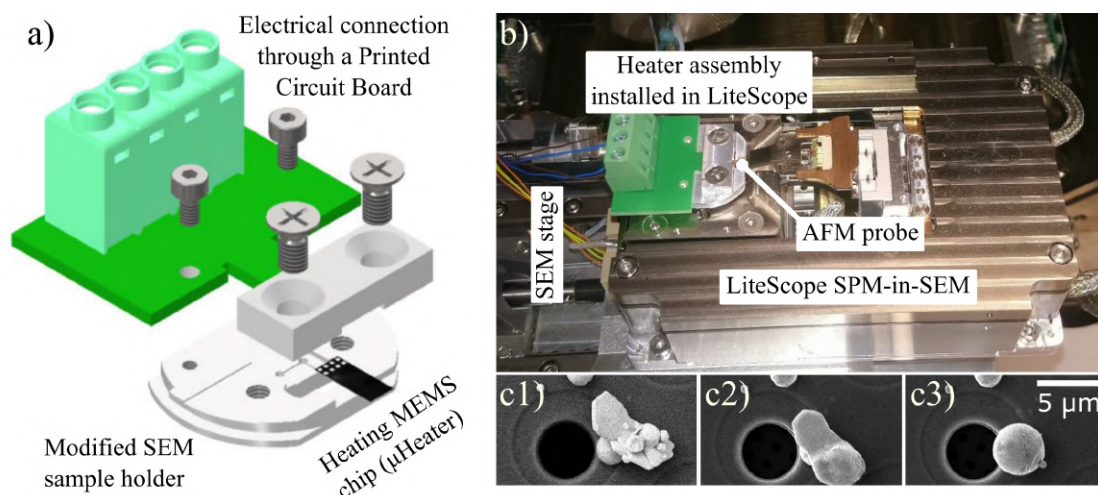

Figure 4.5: Sample heater assembly in LiteScope. **(a)** An exploded projection of the holder I designed for sample heating in LiteScope and **(b)** a real holder installed in the LiteScope microscope. **(c)** Melting of drop-casted gold particles. SEM images of the particles at room temperature (c1), at $1\,060\,°C$ (c2) and at $1\,130\,°C$ (c3). Adapted from [51].

My colleagues (in particular Ing. Kristýna Bukvišová and Ing. Vojtěch Mahel in [53]) have previously identified the optimal way to prepare clean samples and to perform graphene growth by CVD in an SEM chamber. They have also utilised Raman spectroscopy to confirm that this procedure really yields single-layer graphene, which can be identified and imaged by SE detectors in an SEM. The procedure involves a preparation of a golden cube (a *chunk*) by a Plasma FIB, moving it to the µHeater by an SEM manipulator and welding it to the µHeater by GIS deposition. The result of the procedure can be seen in Figure 4.6a. The chunk is then molten by heating it to about $1\,100\,^\circ$C and it reforms into a spherical shape maintained by its surface tension (see Figure 4.6b). The sphere can later be solidified by cooling it down to $950\,^\circ$C (phase transition effects are discussed in the description of Figure 4.7). Whether cooling is performed depends on the desired morphology of the final graphene crystals, as flakes grown on solid metal cannot grow in the way described in Figure 4.3d but they can still be useful for our experiment. It is feasible to first grow several crystals and then stop the growth and melt the metal. During the growth $65\,$Pa of ethylene (C_2H_4) is introduced into the SEM chamber for 5 minutes, during which the microscope is in the environmental SEM (ESEM) mode. The appropriate time was determined heuristically for the particular SEM used to perform this growth (Versa FIB-SEM by Thermo Fisher Scientific). The process is not fully repeatable and sometimes results in the surface being only partially covered by graphene (see Figure 4.6c,d) while on other occasions it gets fully covered by graphene. Since the edges of graphene crystals are of interest, the former option is desirable. The speed of deposition is heavily influenced by the cleanliness of the sample, as a cleaner surface results in faster deposition. Graphene can be partially or fully etched away by introducing ~$10^{-2}\,$Pa of oxygen into the chamber and heating the sample to $950\,^\circ$C. The procedure is shown in Figure 4.7. However, this often causes graphene to become porous (see Figure 4.7c).

4.4 AFM on liquid gold

As we discussed in Section 4.2, SPM measurements on liquid surfaces are challenging. For this reason, I started with the goal of capturing an image of the surface itself. In this experiment, I used a contaminated sample that was no longer useful for graphene growth experiments (see Figure 4.8a,b). All AFM measurements on this type of sample were performed using the Akiyama probe.

An AFM measurement on the first sample at room temperature in Figure 4.8c reveals a surface covered by contaminating particles (possibly oxides or carbides of elements that diffuse into molten gold from the µHeater underneath).

The next step was heating the sample to $1\,100\,^\circ$C and thereby melting the gold. The probe was then approached to the sample with a low setpoint ($2\,$Hz) in order to prevent the tip from pushing too strongly against the surface of liquid gold and dipping inside. An AFM scan was then performed. The results in Figure 4.9 show that the measurement on liquid gold is possible. However, so is the risk of the tip plunging inside the sample with gold solidifying around it (see Figre 4.10a). This issue can arise when the tip pushes too hard against the liquid (the setpoint is too high) or the tip does not follow the surface accurately (wrong setting of the feedback or the scanning is too fast) and it "crashes" inside. In one case, the resonance peak shifted to lower frequency during scanning (although the sphere
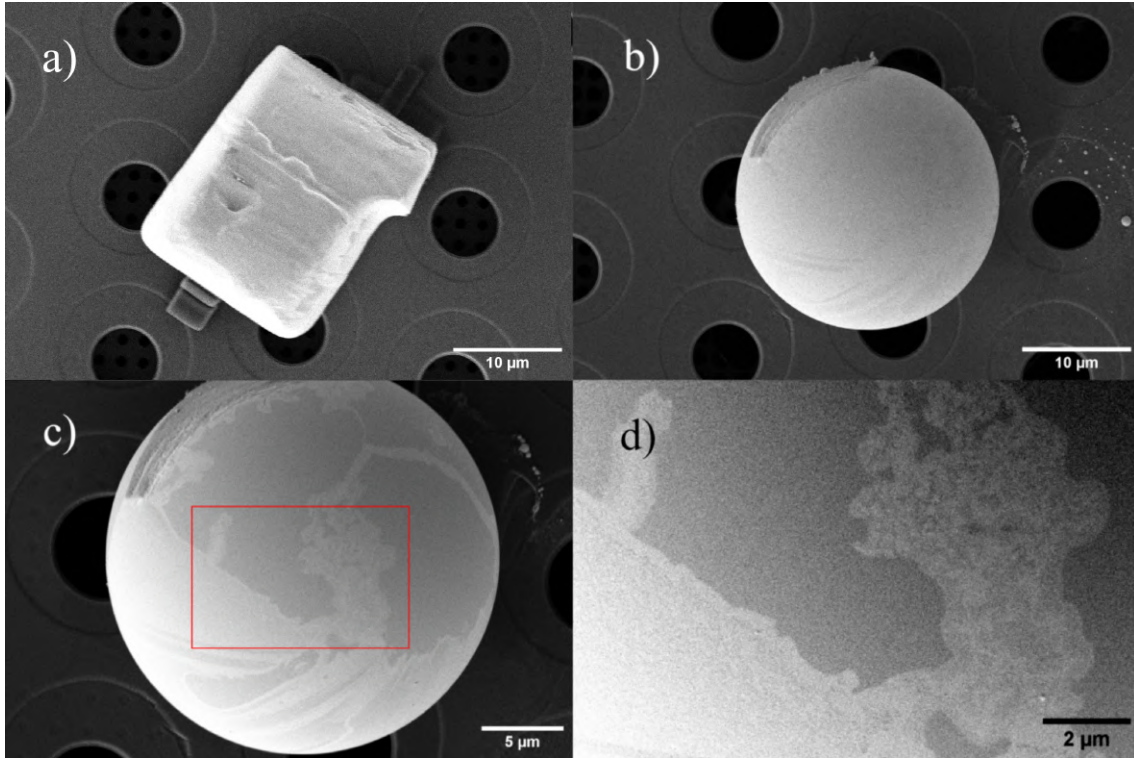
Figure 4.6: Sample preparation for an AFM measurement. All images have been captured by an SEM operating at 5 kV in the SE detection mode. (**a**) A gold chunk manufactured by a Plasma FIB welded to the µHeater by GIS carbon deposition. The sample has been prepared by Ing. Bukvišová. (**b**) The same sample after heating it to 1 100 °C. The contamination at the top left corner is the remaining carbon from GIS deposition. (**c**) The sample after cooling to 950 °C, performing CVD growth by introducing ethylene inside the chamber and reheating it to 1 100 °C. Several large graphene crystals have appeared as well as smaller crystals floating in-between them. The detail of the area marked by the red rectangle is shown in (**d**).

did not stick to the tip in this case). This effect occurs when the probe becomes heavier during the scanning, potentially due to the accumulation of vaporised gold on the tip. Since the setpoint is set relative to the original resonance frequency, this also results in the probe pushing harder against the surface, as the real setpoint in this case is the value set by the user minus the shift in the resonance frequency (which is negative).

There are other processes that can result in the sample being lost or destroyed. A not-yet-molten chunk can also vanish if observed by an SEM at low temperature due to charging, as the surface of the µHeater does not dissipate the electric charge induced by the electron beam at low temperatures. This issue doesn't occur if the sample is observed by the SEM at temperatures higher than 600 °C as silicon nitride can dissipate the charge at such temperatures. The µHeater can be damaged by repeated quick temperature changes and its lifetime is severely shortened by exposure to oxygen at high temperatures. Both of these effects lead to the destruction of the chip shown in Figure 4.10b. If the µHeater's silicon nitride protective layer gets damaged (e.g. by an FIB), gold starts diffusing along the µHeater's surface. The sphere thus disappears and only traces of the sample remain (see Figure 4.10c).
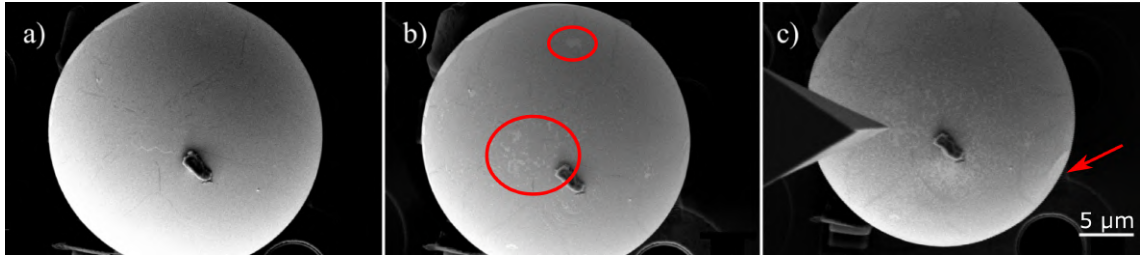
Figure 4.7: Graphene etching caused by oxygen being introduced into the chamber. All images were captured by an SEM operating at 5 kV in the SE detection mode. (**a**) A gold sphere completely covered by graphene. (**b**) Holes (highlighted by red ellipses) start appearing in the graphene layer after the introduction of oxygen into the SEM chamber and (**c**) graphene with porous morphology is created. In (**a**) and (**b**), the sphere is liquid and in (**c**), the sphere is solid. This can be determined in several ways. One way is to calculate the temperature in the middle of the heating spiral from voltage and current supplied to the µHeater and from µHeater's calibration constants provided by the manufacturer. The only issue with this calculation is the temperature hysteresis of the liquid-solid-state transition. Another way is to observe the sample by the SEM as the material increases its volume during melting. The last possibility is to look for facets which are only present on solid gold. Such a facet is highlighted in (**c**) by a red arrow. Scalebar length 5 um.
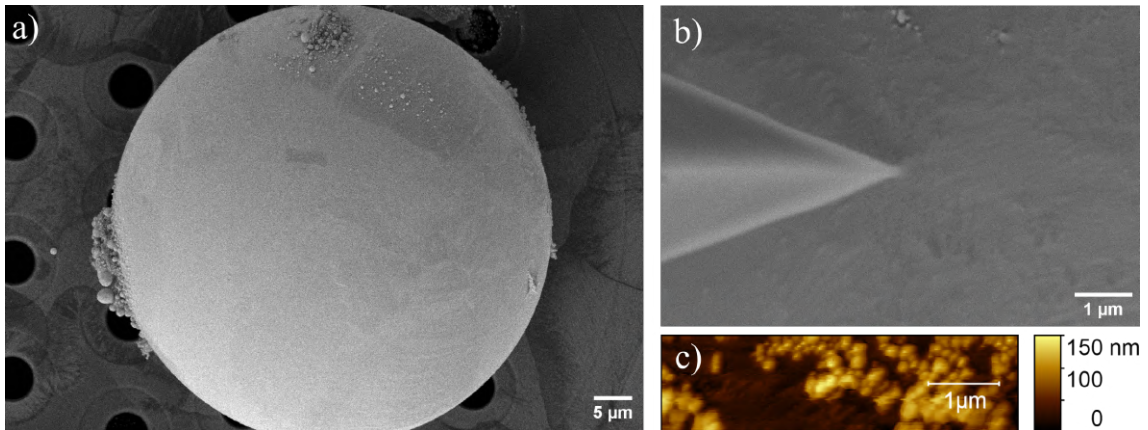

Figure 4.8: The sample used in the first experiment at room temperature. The AFM scan reveals surface contamination. (**a**) An SEM overview of the sample. Although large particles can be seen at the top and on the left side of the sphere, the real issue of the sample are small particles covering the sphere. (**b**) A detail of the surface alongside an AFM tip and (**c**) an AFM topography. The rows in the AFM image have been aligned using the Gwyddion software and the spherical shape of the sphere has been subtracted. A blind estimation of the tip shape has been performed and it was used for the deconvolution of the surface topography. However, it is still possible (even likely) that the tip shape inflates the apparent size of the particles. Sample courtesy of Kristýna Bukvišová.

4.5 AFM of graphene on liquid gold

During the first successful measurement of graphene floating on top of liquid gold, only a few lines were captured before the sample was lost to the phenomenon shown in Figure 4.10a. The result is shown in Figure 4.11. This image tells us two things. First, graphene
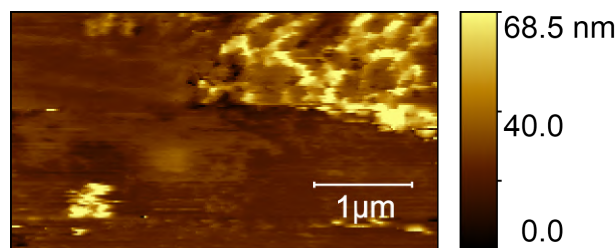
Figure 4.9: Measurement of surface topography by the Frequency Modulated Tapping AFM on a contaminated liquid gold specimen. Small flat areas of clean gold can be seen in the lower section of the image.
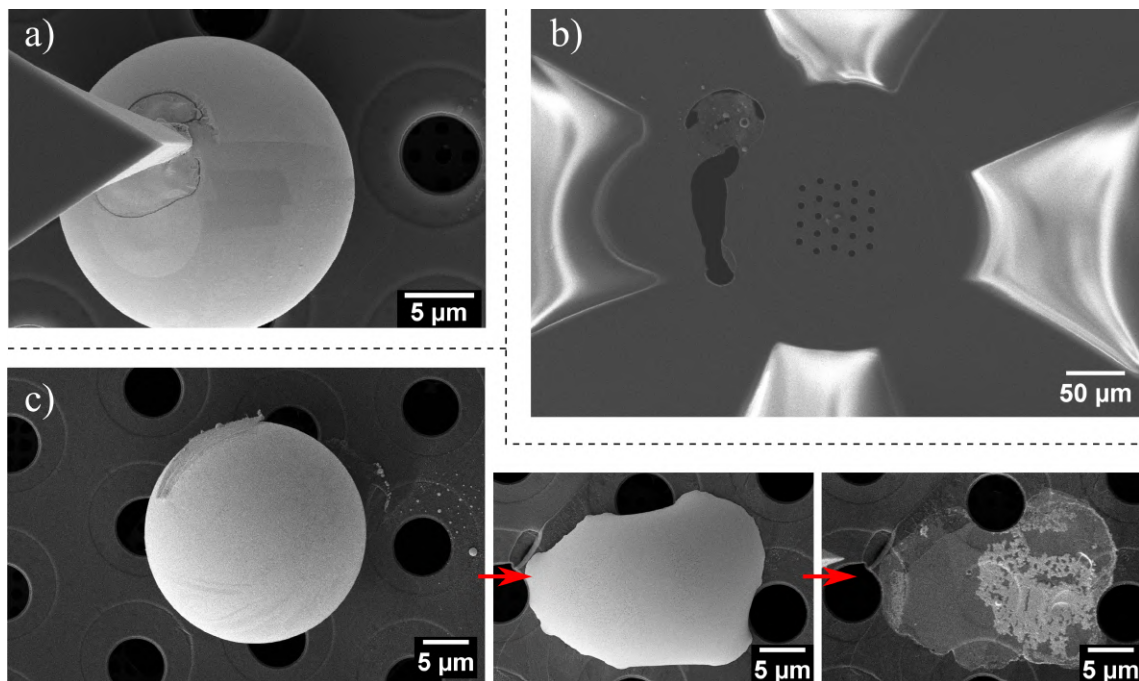

Figure 4.10: Effects that can cause the destruction of the sample. **(a)** Golden sphere can solidify around the AFM tip while ruining the sample and the tip. **(b)** The heater can be damaged either by repeated quick temperature changes or by degradation induced by heating in an oxygen rich atmosphere. The chunk can also vanish if observed by an SEM at low temperature because of charging. In such cases, only the residue of the GIS deposit remains (see the centre of the panel (b)). **(c)** An instance when gold was diffusing along the surface and the sample slowly (over the course of several hours, time increases as indicated by red arrows) disappeared.

is not significantly elevated above the level of the liquid (~6 nm at most). Second, the meniscus at the edges of graphene flakes (and consequently the range of capillary forces) is at most on the order of tens of nanometres long. However, it is important to take into consideration the convolution of the real topography with the AFM tip. Although the Akiyama probe should have a tip radius smaller than 15 nm, it is a common effect that this value changes during measurements as the material from the sample deposits on the tip and its shape progressively changes.

In order to achieve a better understanding of the sample, more measurements were needed. The next one revealed a dependence of the height difference between gold and graphene
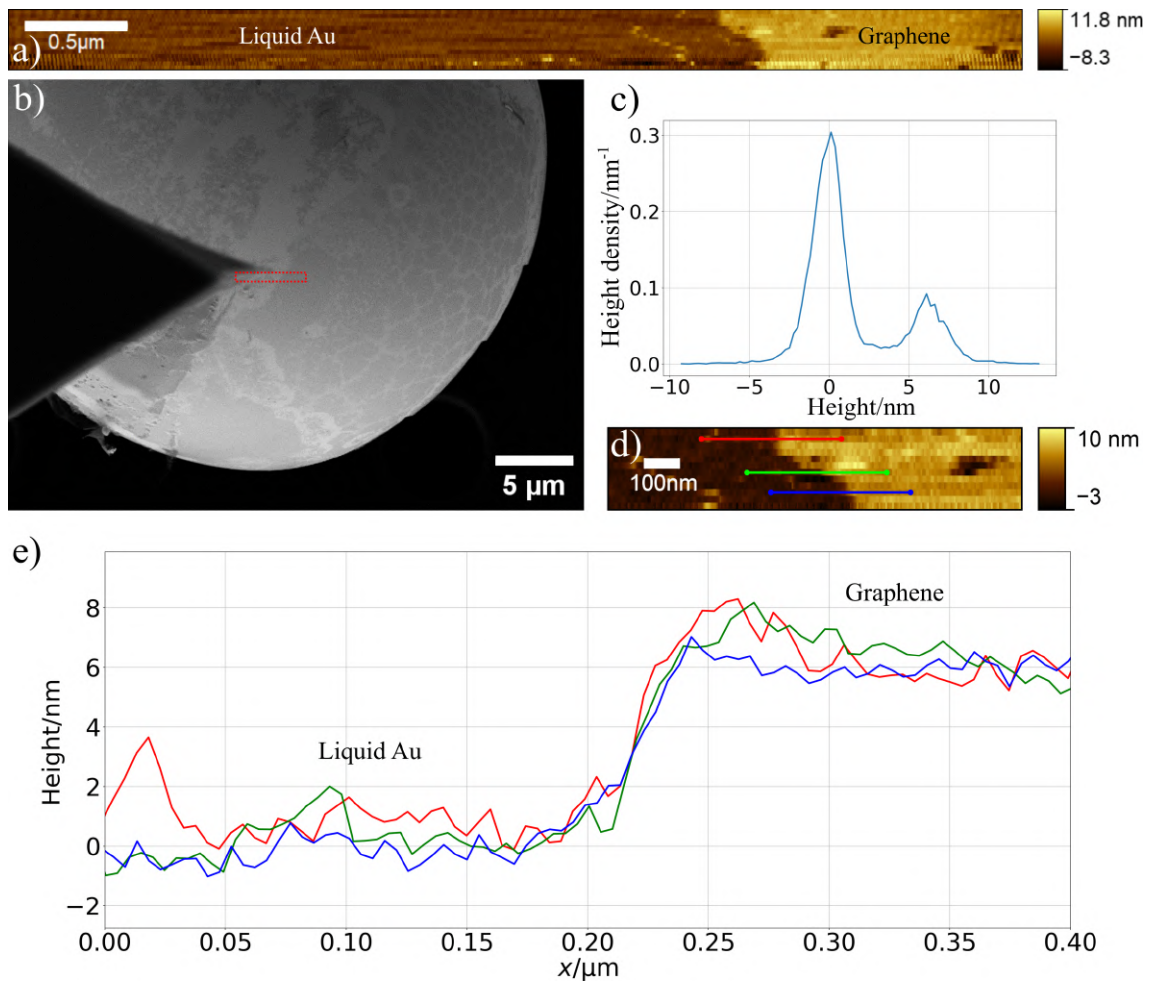
Figure 4.11: The first successful measurement of graphene on liquid gold. (**a**) The measured topography after row alignment and subtraction of the shape of the sphere. The z-axis has been shifted to set the mean level of liquid gold to 0 nm. Measurement was performed with the setpoint of 6 Hz. (**b**) An SEM image of the sample after CVD growth prior to AFM measurement. The red rectangle marks the region scanned by the AFM. Notice the slight difference in the morphology of graphene between the AFM and SEM measurements. It is caused by a slow movement of graphene during AFM scanning. (**c**) A height histogram extracted from the panel (a). Two distinct peaks at heights 0.0 nm (liquid gold) and 6.0 nm (graphene) can be observed. (**d**) Detail of the graphene edge from the panel (a). Row alignment and z-axis shift have been performed independently for this image as the mean hight of liquid gold in this area slightly (by 0.17 nm) differs from the whole image. The profiles in (**e**) are extracted along the red, green, and blue line in the panel (d). The profiles exhibit a pronounced step at the boundary of the graphene crystal. Sample courtesy of Kristýna Bukvišová.

(the step height) on the measurement's setpoint. As discussed in Section 2.1, the setpoint is the value of the feedback signal (in this case the frequency shift) that the microscope is maintaining. It is approximately linearly proportional [11] to the force exerted on the sample. The higher the setpoint, the larger the force. However, the setpoint is not the only thing that affects the magnitude of the force exerted on the sample. It also depends heavily on the probe's amplitude of oscillations [11] and the specific AFM probe, as there
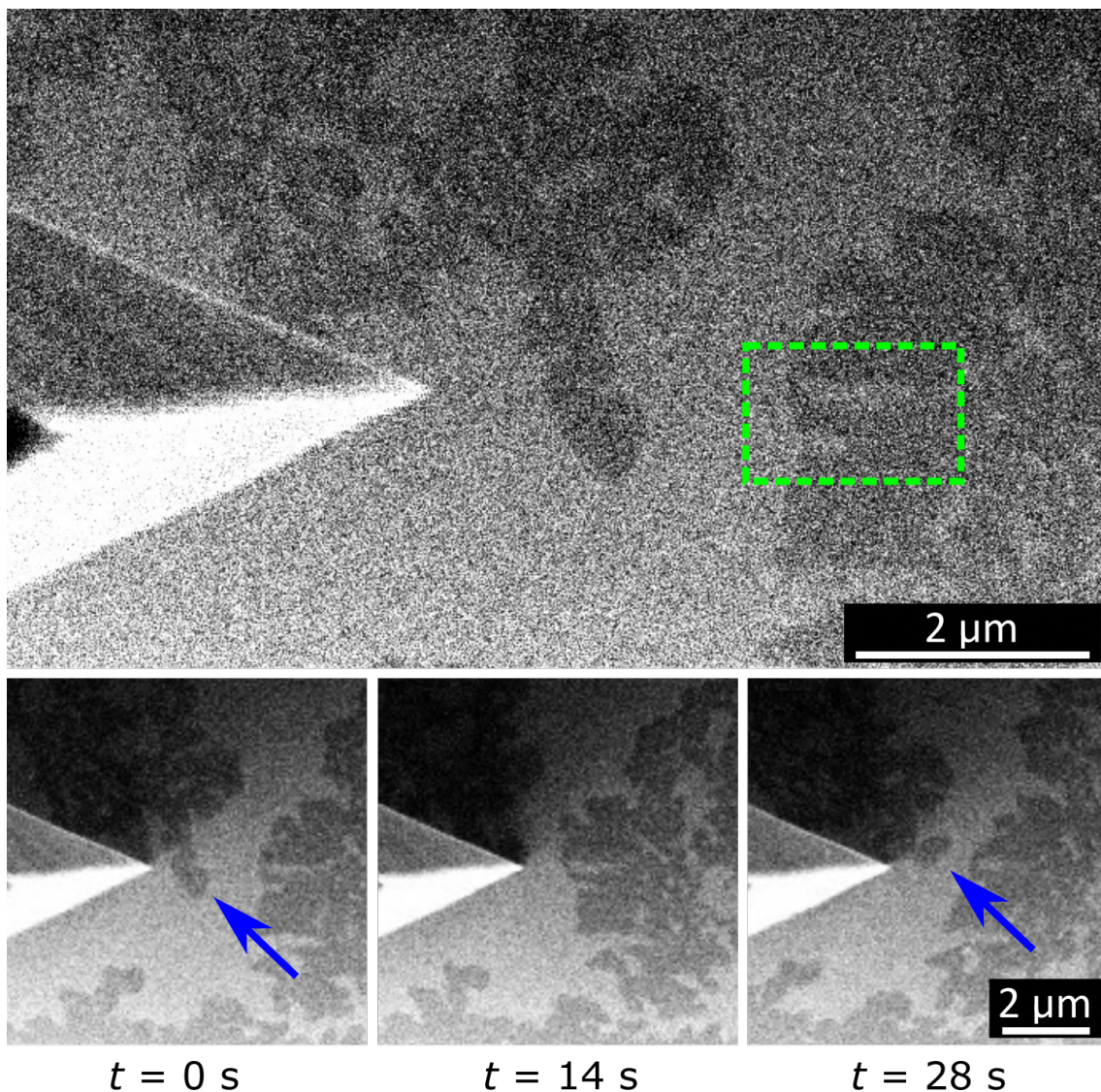
Figure 4.12: Scanning induced damage. In the upper part of the Figure, there are two areas highlighted by a green rectangle. In these areas, AFM scanning had been previously performed and these scars are presumably places where graphene has been removed. In the lower part of the Figure, there are three SEM images taken consecutively during one line-scan performed with the AFM probe (trace and retrace). A part of graphene dendrite (marked by a blue arrow) can be observed to be "cut-off" from the rest of the graphene structure. Note that the AFM scanning deforms the SEM image in the horizontal direction as the sample moves during scanning (LiteScope is a so-called scanning sample AFM). Time per frame is 14 s.

can be significant differences between individual tips. Another observed effect was the removal of graphene in the scanned area. This effect (see Figure 4.12) might be explained as either mechanical damage from tip-induced forces or as a process similar to local anodic oxidation. The oxidation hypothesis is supported by the fact that the tip-induced damage was only observed shortly after the pumping of the SEM chamber (on the order of tens of minutes after switching from the oxygen/ethylene ESEM mode back to High Vacuum SEM). The amplified electric field around the tip could decompose the residual oxygen, which subsequently reacted with graphene.

44

The Figure 4.13 shows the next measurement during which the setpoint was changed from 5 Hz to 2 Hz. There is a significant difference between the rows measured at 5 Hz (larger tip-sample forces) and at 2 Hz (smaller tip-sample forces). The height of the step between gold and graphene gets smaller with a decrease in setpoint. A possible explanation is that the tip slightly dips inside the molten gold during scanning. This effect would explain the height difference between the surface of gold and the graphene crystal. When the setpoint is low (lower force), this height difference decreases.

It is also possible to analyse mean heights in separate sections of the image. The result is shown in Figure 4.14. This measurement is approaching the limits of the insights that can be provided by the AFM. On one hand, we could conclude that if the sample could be measured with the setpoint of 0 Hz (e.g. without any force exerted on the sample), there would be no height difference between molten gold and graphene. On the other hand, we should consider that the evaluation of the thickness of graphene by an AFM is generally a complicated task. Graphene is a 2D structure and tip-sample interactions can significantly affect the height we get from the AFM image. This topic has been widely discussed since the discovery of graphene. For example, in [54] they calculated the height of multilayer graphene h as $h = n \cdot t + t_0$, where n is the number of layers, $t = 0.33$ nm is approximately equal to the interlayer distance in graphite and $t_0 = 0.35$ nm is an *instrumental offset*. The equation holds quite well, as they found the height of a single layer graphene to be 0.7 nm. In [55] the phenomenon is explained more thoroughly and it is claimed that unless special care is taken, the step heights obtained can vary significantly among images. Considering that our system is even more complicated as it is located on a liquid, we will limit ourselves to concluding that the meniscus around the graphene crystals (if it exists at all) is not significant in size and it does not support the existence of a capillary force with a range on the order of microns as suggested in [47]. The images from Figures 4.11 and 4.13 are also shown in Supplement B without the subtraction of the spherical background to demonstrate that this operation neither obscures the presence of the meniscus nor affects the conclusion in other ways.

Finally, a large scan performed with the setpoint of 5 Hz is shown in Figure 4.15. Note that the setpoint is not the only parameter affecting the magnitude of the tip-sample force and the step-height cannot therefore be reproduced only by using the same setpoint in different measurements.
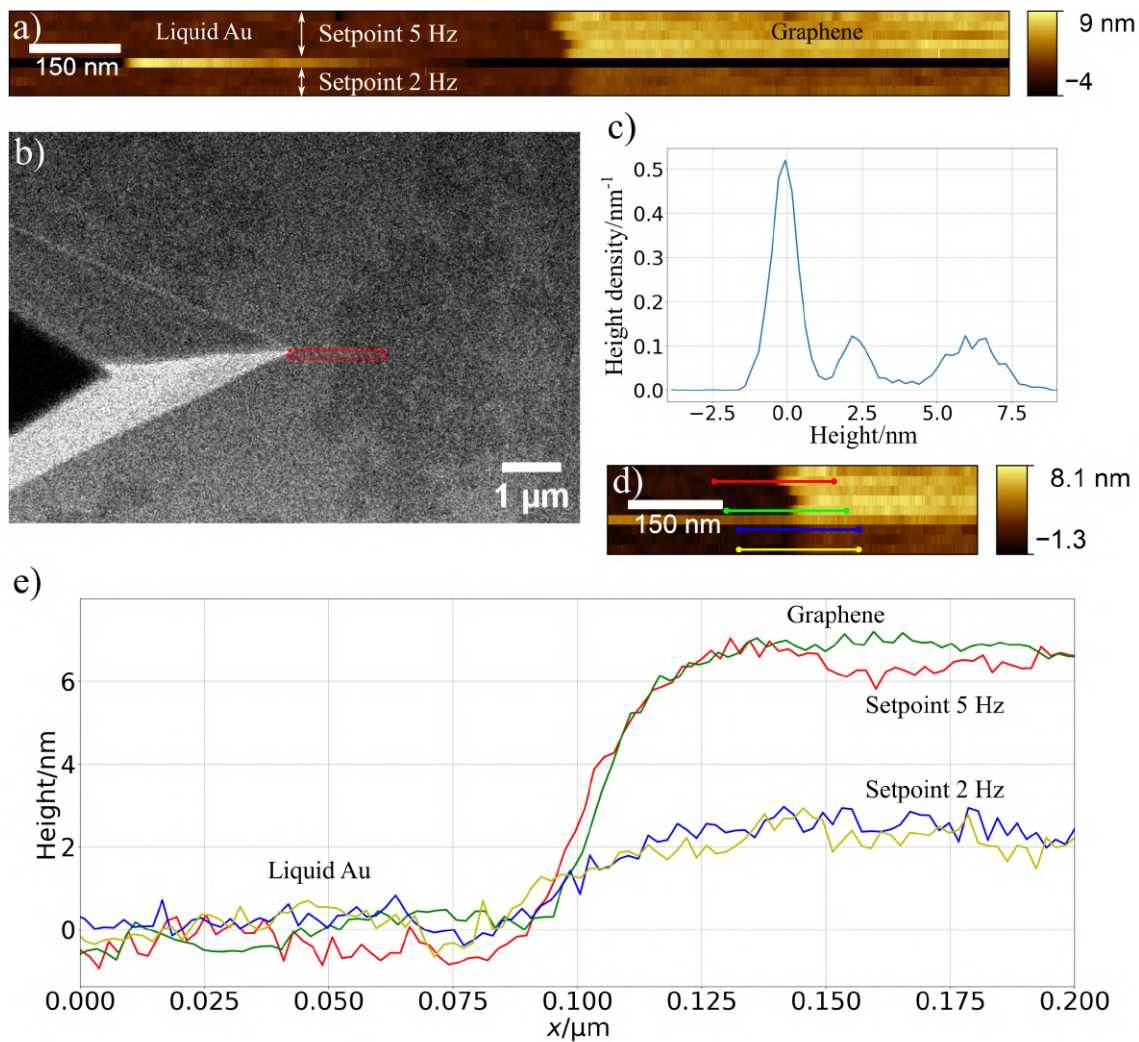
Figure 4.13: Measurement of graphene on liquid gold with an intermediate change in setpoint. First five rows had been measured with the setpoint of 5 Hz, on row six the setpoint was changed to 2 Hz, which resulted in a faulty line, and subsequently three more rows have been measured. (**a**) The measured topography after row alignment and after subtraction of the shape of the sphere. The z-axis has been shifted to set the mean level of liquid gold to 0 nm. The area of molten gold was used for the row alignment (therefore gold has the same height in all rows), although alternatively it would also make sense to do the alignment in the area with graphene and then the difference in height between lines (the vertical step) would be observed in the area of liquid gold (in the left side of the image) and graphene would be flat. (**b**) An SEM image of the sample. The red rectangle marks the region scanned by the AFM. (**c**) A height histogram extracted from the panel (a). Three distinct peaks at heights 0.0 nm (liquid gold), 2.2 nm (graphene at the setpoint 2 Hz) and 6.0 nm (graphene at the setpoint 5 Hz) can be observed. (**d**) Detail of the graphene edge from the panel (a). Row alignment and z-axis shift have been performed independently for this image as the mean height of liquid gold in this area slightly (by 0.03 nm) differs from the whole image. The profiles in (**e**) are extracted along the red, green, blue, and yellow line in the panel (d). The profiles exhibit a pronounced step at the boundary of the graphene crystal, and the step height varies with the chosen setpoint. Sample courtesy of Kristýna Bukvišová.
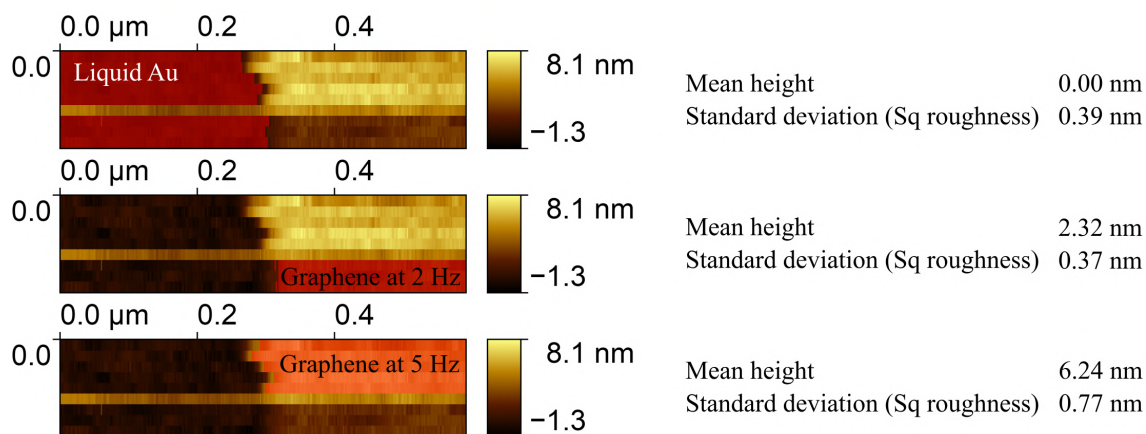
Figure 4.14: Height analysis of individual areas in the measurement with a change of setpoint. The mean heights have been calculated from the areas highlighted by red masks. The evaluation shows a significant difference between the mean height of graphene measured with setpoint 2 Hz and 5 Hz.
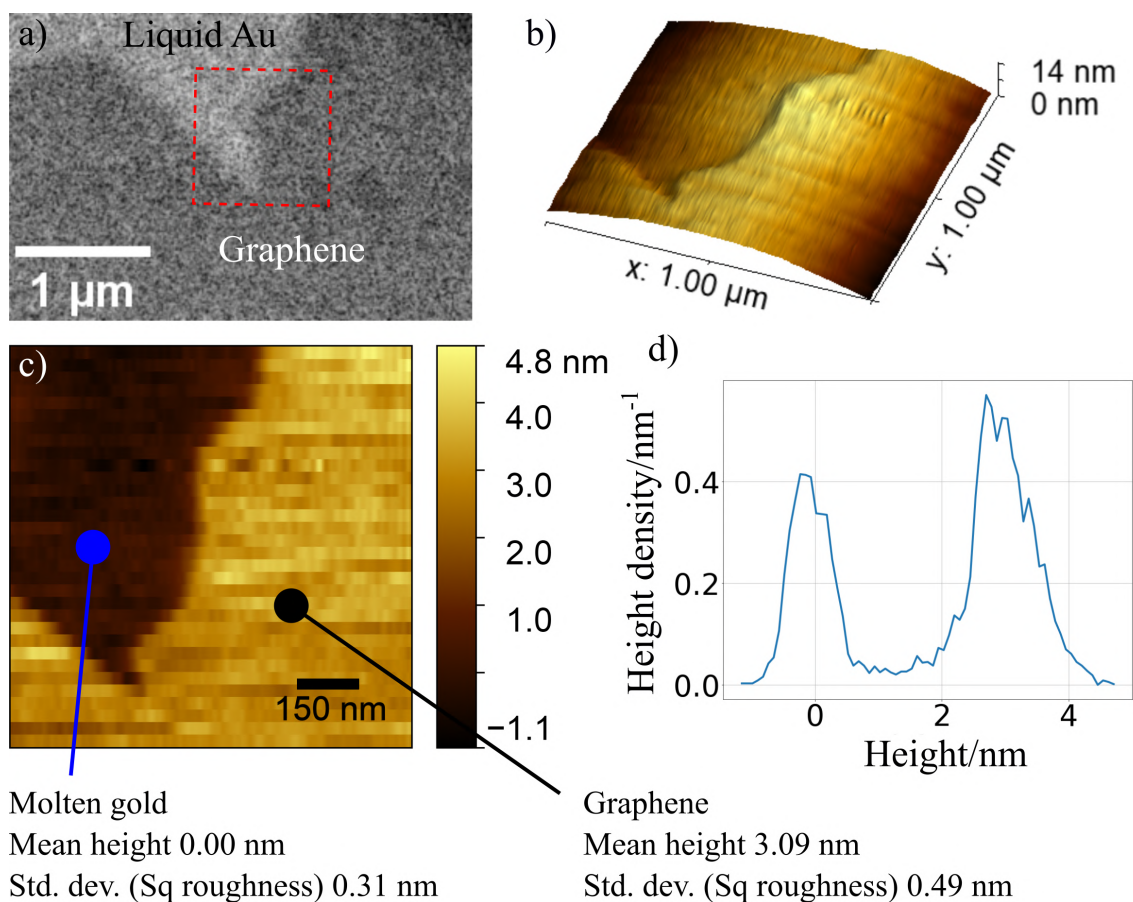
Figure 4.15: An AFM scan depicting graphene on molten gold taken with the setpoint of 5 Hz. (**a**) An SEM image of the scanned area after the AFM scan. The red square marks the scan area. The AFM image after row alignment, (**b**) before and (**c**) after the subtraction of the spherical shape. (**d**) A height histogram extracted from the panel (c). Note that the morphology of graphene slightly differs between the AFM and SEM images as a slow graphene growth was still occurring at this point. The SEM image also proves that graphene was not damaged by the AFM scan. Sample courtesy of Kristýna Bukvišová.

5 Conclusions

In this diploma thesis, I aimed to explore several use-cases for in-situ probe microscopy. In the opening chapter, I summarised the operating principles of the analytical techniques which I used in the thesis. These techniques mainly include the basic and one of the advanced modes of scanning probe microscopy, which can provide information about the sample topography and conductive properties. Another vital analytical technique described in the opening chapter is scanning electron microscopy.

First, I focused on research in the field of energy storage. I summarised important information about the operating principles of batteries and listed their most important types while paying increased attention to solid state batteries, which are generally considered to be one of the most promising technologies enabling advances in energy storage. As I used the LiteScope SPM-in-SEM microscope, I benefited from the fact that I was able to observe the sample simultaneously with the probe and the electron beam. The integration into a scanning electron microscope also proved to be very beneficial for the experiments with battery materials because most of them are sensitive to air exposure.

I initially attempted to capture the development of an interface between the negative electrode and liquid electrolyte in a Li-ion battery. This measurement turned out to be complicated and ultimately unsuccessful. However, the measurement is still valuable because it demonstrates the feasibility of performing atomic force microscopy measurements with the Akiyama probe inside a liquid.

My following experiments were focused on proof-of-concept measurements on solid state batteries and they were performed in collaboration with my colleague Bc. Jan Kramář. In the first type of experiment, we investigated the electrodeposition of lithium in a half-cell (a battery with the positive electrode missing). We used the probe tip as a current collector and electrodeposited lithium pillars on top of the solid electrolyte. As both lithium and the electrolyte are air-sensitive, we utilised an accessory called CleanConnect, which allows samples to be transferred between the storage glovebox and the electron microscope without any exposure to air. We were able to perform the deposition repeatably, with lithium migrating from the negative electrode to the probe and subsequently fully returning to the negative electrode. The surprising finding was that the initiation voltage for lithium deposition was not consistent and it changed between individual measurements.

The second type of experiment followed on the idea of lithium transport. We attempted to create a small battery cell by drop-casting MXene particles on the half-cell and then using the tip of the probe as a current collector. We hypothesised that it would be possible to detect the expansion of the particles during cycling using LiteScope and a scanning electron microscope or to identify variations between horizontally and vertically stacked particles. Unfortunately, we observed neither of these effects. It is also possible that the lithium ions did not embed themselves inside the MXene particles and they were only deposited underneath the MXenes, since we observed no morphological changes by the electron microscope. More research into this topic would be required to explain this process in its entirety.

In the second part of the thesis, I moved to the topic of graphene on molten metals. In an effort to explain the force interactions that take place between flakes of graphene floating on top of molten metals, I have followed the work of my colleagues. The synthesis of

graphene on molten metals represents a promising method for producing large graphene sheets devoid of grain boundaries, making this system a significant research objective. In the past, researchers have speculated about the capillary force acting between the flakes. As the presence of such force requires the existence of a meniscus around the flakes, my aim was to investigate the topography of these flakes. I employed a microelectromechanical heating element to liquefy small gold cubes and I grew graphene on them via chemical vapour deposition. Subsequently, I utilised frequency modulated tapping atomic force microscopy to measure the topography of these flakes. My measurements do not support the existence of a significant meniscus (larger than units of nanometres) around these flakes.

Beyond the study of the graphene-on-liquid system, this measurement also holds interest from the instrumentation perspective. Scanning probe microscopy on liquid surfaces is generally considered to be difficult, and it is important to know that it is possible on liquid gold under the conditions described in this thesis. Another interesting effect was the influence of the tip-sample force. The measured step height between graphene and liquid gold increased with higher force. I have also listed the problems we encountered.

My experiments showcase the potential that LiteScope and probe microscopy in general hold in the field of in-situ experiments. The toolkit of scanning probe microscopy offers techniques with potential for utilisation in dynamic in-situ experiments.

Bibliography

[1] J. T. McKeown, et. al., *Imaging Irreversible Transformations with Movie-Mode Dynamic Transmission Electron Microscopy*, Microscopy and Microanalysis, vol. 21, issue S3, p. 1853 - 1854, `https://doi.org/10.1017/S1431927615010041`

[2] EPFL, *High Speed Atomic Force Microscopy* [online], EPFL, 2023, Accessed May 14, 2023. Available at `https://www.epfl.ch/labs/lbni/research/instrumentation/instrumentation-smallleverhead/`

[3] B. Voigtländer, *Atomic Force Microscopy: Second Edition*, Springer, 2019, p. 8 - 10, ISBN: 9783030136543

[4] U. Celano, *Electrical Atomic Force Microscopy for Nanoelectronics*, Springer, 2019, p. 30 - 36, ISBN: 9783030156121

[5] J. Giorgi, *NC-AFM and XPS Investigation of Single-crystal Surfaces Supporting Cobalt (III) Oxide Nanostructures Grown by a Photochemical Method*, Master's thesis, University of Ottawa, 2012, p. 15

[6] B. J. Ford, D. C. Joy, S. Bradbury, *scanning electron microscope* [online], Britannica, 2012, Accessed March 20, 2024. Available at `https://www.britannica.com/technology/scanning-electron-microscope`

[7] J. Goldstein, et. al., *Scanning Electron Microscopy and X-Ray Microanalysis. THIRD EDITION.*, Springer, 2003, p. 21 - 25, ISBN: 9781461502159

[8] L. A. Giannuzzi, et. al., *Introduction to Focused Ion Beams: Instrumentation, Theory, Techniques and Practice*, Springer, 2004, p. 1 - 12, 54 - 55, 61, ISBN: 9780387231167

[9] A. Wolff, *Focused ion beams: An overview of the technology and its capabilities* [online], Wiley Magazine, 2020, Accessed March 21, 2024. Available at `https://analyticalscience.wiley.com/content/article-do/focused-ion-beams-overview-technology-and-its-capabilities`

[10] NenoVision, *LiteScope AFM-in-SEM* [online], NenoVision, 2024, Accessed April 6, 2023. Available at `https://www.nenovision.com/products/litescope-afm-in-sem`

[11] Akiyama-Probe, *Akiyama-Probe* [online], Nanosensors, 2023, Accessed May 1, 2024. Available at `https://www.akiyamaprobe.com/`

[12] IUPAC Gold Book, *cathode* [online], IUPAC, 2019, Accessed January 31, 2024. Available at `https://doi.org/10.1351/goldbook.C00905`

[13] J. T. Frith, M. J. Lacey, U. Ulissi, *A non-academic perspective on the future of lithium-based batteries*, Nature Communications, 2023, vol. 14, p. 420. Available at `https://doi.org/10.1038/s41467-023-35933-2`

[14] W. Liu, T. Placke, K.T. Chau, *Overview of batteries and battery management for electric vehicles*, Energy Reports, 2022, vol. 8, p. 4058 - 4084. Available at `https://doi.org/10.1016/j.egyr.2022.03.016`

[15] IUPAC Gold Book, *standard electrode potential, E* [online], IUPAC, 2019, Accessed January 28, 2024. Available at `https://doi.org/10.1351/goldbook.S05912`

[16] K. E. Aifantis, S. A. Hackney, R. V. Kumar, *High Energy Density Lithium Batteries: Materials, Engineering, Applications*, Wiley, 2010, p. 4 - 7, 14 - 15, ISBN: 9783527630011

[17] K. P. Birke, et. al., *Modern Battery Engineering: A Comprehensive Introduction*, World Scientific, 2019, p. 1 - 14, ISBN: 9789813272170

[18] G. Pistoia, *Lithium-Ion Batteries - Advances and Applications*, Elsevier, 2014, p. 1 - 20, ISBN: 9780444595164

[19] D. Castelvecchi, *Electric cars and batteries: how will the world produce enough?*, Nature, 2021, vol. 596, p. 336 - 339, `https://doi.org/10.1038/d41586-021-02222-1`

[20] C. Buechel, L. Bednarski, S. Wietlisbach, *As lithium-ion battery materials evolve, suppliers face new challenges* [online], S&P Global Commodity Insights, 2021, Accessed November 13, 2023. Available at `https://www.spglobal.com/commodityinsights/en/ci/research-analysis/lithiumion-battery-materials-evolve-suppliers-face-new-challenges.html`

[21] FreeingEnergy, *Energy Fact – The cost of batteries decline as manufacturing capacities increase* [online], FreeingEnergy, 2021, Accessed November 12, 2023. Available at `https://www.freeingenergy.com/facts/learning-lithium-ion-batteries-economies-price-decline-g202/`

[22] Q. Zhen, et. al., *Nanostructured Materials for Next-Generation Energy Storage and Conversion: Advanced Battery and Supercapacitors*, Springer, 2019, p. 147 - 150, 174, ISBN: 9783662586730

[23] W. M. Haynes, et al., *CRC Handbook of Chemistry and Physics, 97th Edition*, CRC Press, 2016, p. 14 - 17, ISBN: 9781498754286

[24] W. Zhao, J. Yi, P. He, et al., *Solid-State Electrolytes for Lithium-Ion Batteries: Fundamentals*, Electrochemical Energy Reviews, 2019, vol. 2, p. $574 - 605$, `https://doi.org/10.1007/s41918-019-00048-0`

[25] R. K. Gupta, et al., *Solid State Batteries Volume 1: Emerging Materials and Applications*, ACS Publications, 2022, p. 1 - 15, ISBN: 9780841297678

[26] A. v. Cresce, et. al., *In Situ and Quantitative Characterization of Solid Electrolyte Interphases*, Nano Letters, 2014, vol. 14, issue 3, p. 1405 - 1412, `https://doi.org/10.1021/nl404471v`

[27] TipsNano, *TGQ1* [online], TipsNano, 2024, Accessed May 21, 2023. Available at `https://tipsnano.com/catalog/calibration/tgq1/`

[28] M. Leither, et. al., *Atomic Force Microscopy Imaging in Turbid Liquids: A Promising Tool in Nanomedicine*, Sensors, 2020, vol. 20, issue 13, p. 3715, `https://doi.org/10.3390/s20133715`

[29] C. Shen, et. al., *Unraveling the mechanism of ion and electron migration in composite solid-state electrolyte using conductive atomic force microscopy*, Energy Storage Materials, 2021, vol. 39, p. 271 - 277, `https://doi.org/10.1016/j.ensm.2021.04.028`

[30] G. McConohy, et. al., *Mechanical regulation of lithium intrusion probability in garnet solid electrolytes*, Nature Energy, 2023, vol. 8, p. 241 - 250, `https://doi.org/10.`

1038/s41560-022-01186-4

[31] A. L. Santhosha, *The Indium-Lithium Electrode in Solid-State Lithium-Ion Batteries: Phase Formation, Redox Potentials, and Interface Stability*, Batteries & Supercaps, 2021, vol. 4, issue 10, p. 1654 - 1654, `https://doi.org/10.1002/batt.201800149`

[32] Thermo Fisher Scientific, *CleanConnect Sample Transfer System* [online], Thermo Fisher Scientific, 2023, Accessed May 14, 2023. Available at `https://assets.thermofisher.com/TFS-Assets/MSD/Datasheets/cleanconnect-datasheet-ds0378.pdf`

[33] M. Magnuson, M. Mattesini, *Chemical bonding and electronic-structure in MAX phases as viewed by X-ray spectroscopy and density functional theory*, Thin Solid Films, 2017, vol. 621, p. 108 - 130, `https://doi.org/10.1016/j.tsf.2016.11.005`

[34] D. Wang, et. al., *Direct synthesis and chemical vapor deposition of 2D carbide and nitride MXenes*, Science, 2023, vol. 379, issue 6638, p. 1242 - 1247, `https://doi.org/10.1126/science.add9204`

[35] M. Naguib, et. al., *25th Anniversary Article: MXenes: A New Family of Two-Dimensional Materials*, Advanced Materials, 2014, vol. 26, issue 7, p. 992 - 1005, `https://doi.org/10.1002/adma.201304138`

[36] O. Salim, et. al., *Introduction to MXenes: synthesis and characteristics*, Materials Today Chemistry, 2019, vol. 14, p. 100191, `https://doi.org/10.1016/j.mtchem.2019.08.010`

[37] R. Akhter, S. S. Maktedar, *MXenes: A comprehensive review of synthesis, properties, and progress in supercapacitor applications*, Journal of Materiomics, 2023, vol. 9, issue 6, p. 1196 - 1241, `https://doi.org/10.1016/j.jmat.2023.08.011`

[38] M. Greaves, S. Barg, M. A. Bissett, *MXene-Based Anodes for Metal-Ion Batteries*, Batteries & Supercaps, 2019, vol. 3, issue 3, p. 214 - 235, `https://doi.org/10.1002/batt.201900165`

[39] W. Zhao, *Hierarchically structured Ti3C2Tx MXene paper for Li-S batteries with high volumetric capacity*, Nano Energy, 2021, vol. 86, p. 106120, `https://doi.org/10.1016/j.nanoen.2021.106120`

[40] A. Byeon, et. al., *Two-Dimensional Titanium Carbide MXene As a Cathode Material for Hybrid Magnesium/Lithium-Ion Batteries*, ACS Applied Materials & Interfaces, vol. 9, issue 5, p. 4296 - 4300, `https://doi.org/10.1021/acsami.6b04198`

[41] R. Battistelli, *Tuning the magnetic properties of Iron Phthalo-cyanines on intercalated Graphene via alkali metal doping*, Master's thesis, Sapienza – Università di Roma, 2019, p. 12

[42] N. Peres, *Graphene: New physics in two dimensions*, Europhysics News, 2009, vol. 40, issue 3, p. 17 – 20, `https://doi.org/10.1051/epn/2009501`

[43] K. I. Bolotin, et. al., *Ultrahigh electron mobility in suspended graphene*, Solid State Communications, 2008, vol. 146, issues 9 - 10, p. 351 – 355, `https://doi.org/10.1016/j.ssc.2008.02.024`

[44] A. K. Geim, K. S. Novoselov, *The rise of graphene*, Nature Materials, 2007, vol. 6,

issue 3, p. 183 – 191, `https://doi.org/10.1038/nmat1849`

[45] H. Liu, Y. Liu, *Controlled Chemical Synthesis in CVD Graphene*, Physical Sciences Reviews, 2017, vol. 2, issue 4, p. 20160107, `https://doi.org/10.1515/psr-2016-0107`

[46] D. Geng, B. Wu, Y. Guo, *Uniform hexagonal graphene flakes and films grown on liquid copper surface*, PNAS, 2012, vol. 109, issue 21, p. 7992 - 7996, `https://doi.org/10.1073/pnas.1200339109`

[47] M. Jankowski, et. al., *Real-Time Multiscale Monitoring and Tailoring of Graphene Growth on Liquid Copper*, ACS Nano, 2021, vol. 15, issue 6, p. 9638 - 9648, `https://doi.org/10.1021/acsnano.0c10377`

[48] P. G. Hartley, et. al., *Surface Forces and Deformation at the Oil-Water Interface Probed Using AFM Force Measurement*, Langmuir, 1999, p. 7282 - 7289, `https://doi.org/10.1021/la9817563`

[49] L. Costa, et. al., *Liquid–Liquid Interfacial Imaging Using Atomic Force Microscopy*, Advanced Materials Interfaces, 2017, vol. 4, issue 16, p. 1700203, `https://doi.org/10.1002/admi.201700203`

[50] C. Bruckner-Lea, et. al., *Scanning Tunneling Microscopy on a Mercury Sessile Drop*, Langmuir, 1993, vol. 9, issue 12, p. 3612–3617, `https://doi.org/10.1021/la00036a042`

[51] M. Patočka, *Implementace ohřevu vzorku do mikroskopu atomárních sil*, Bachelor's thesis, Brno University of Technology, 2022

[52] Britannica, *gold* [online], Britannica, 2024, Accessed March 4, 2024. Available at `https://www.britannica.com/science/gold-chemical-element`

[53] V. Mahel, *Optimalizace růstu grafenu na kovových substrátech v rastrovacím elektronovém mikroskopu*, Bachelor's thesis, Brno University of Technology, 2021

[54] A. Gupta, et. al., *Raman Scattering from High-Frequency Phonons in Supported n-Graphene Layer Films*, Nano Letters, 2006, vol. 6, issue 12, p. 2667 - 2673, `https://doi.org/10.1021/nl061420a`

[55] P. Nemes-Incze, et. al., *Anomalies in thickness measurements of graphene and few layer graphite crystals by tapping mode atomic force microscopy*, Carbon, 2008, vol. 46, issue 11, p. 1435 - 1442, `https://doi.org/10.1016/j.carbon.2008.06.022`

List of abbreviations and symbols

AFM	Atomic Force Microscopy (Microscope)
BSE	Backscattered Electron
C-AFM	Conductive Atomic Force Microscopy (Microscope)
CVD	Chemical Vapour Deposition
EFM	Electric Force Microscopy
ESEM	Environmental Scanning Electron Microscopy (Microscope)
GFET	Graphene Field Effect Transistor
GIS	Gas Injection System
LiTFSI	Lithium bis(trifluoromethanesulfonyl)imide
NCA	Nickel Cobalt Aluminium
NMC	Nickel Manganese Cobalt
NPC	NenoProbe Conductive
SE	Secondary Electron
SEI	Solid Electrolyte Interface
SEM	Scanning Electron Microscopy (Microscope)
SEP	Standard Electrode Potential
SPM	Scanning Probe Microscopy (Microscope)
SSB	Solid-State Battery
SSE	Solid-State Electrolyte
STM	Scanning Tunnelling Microscopy (Microscope)

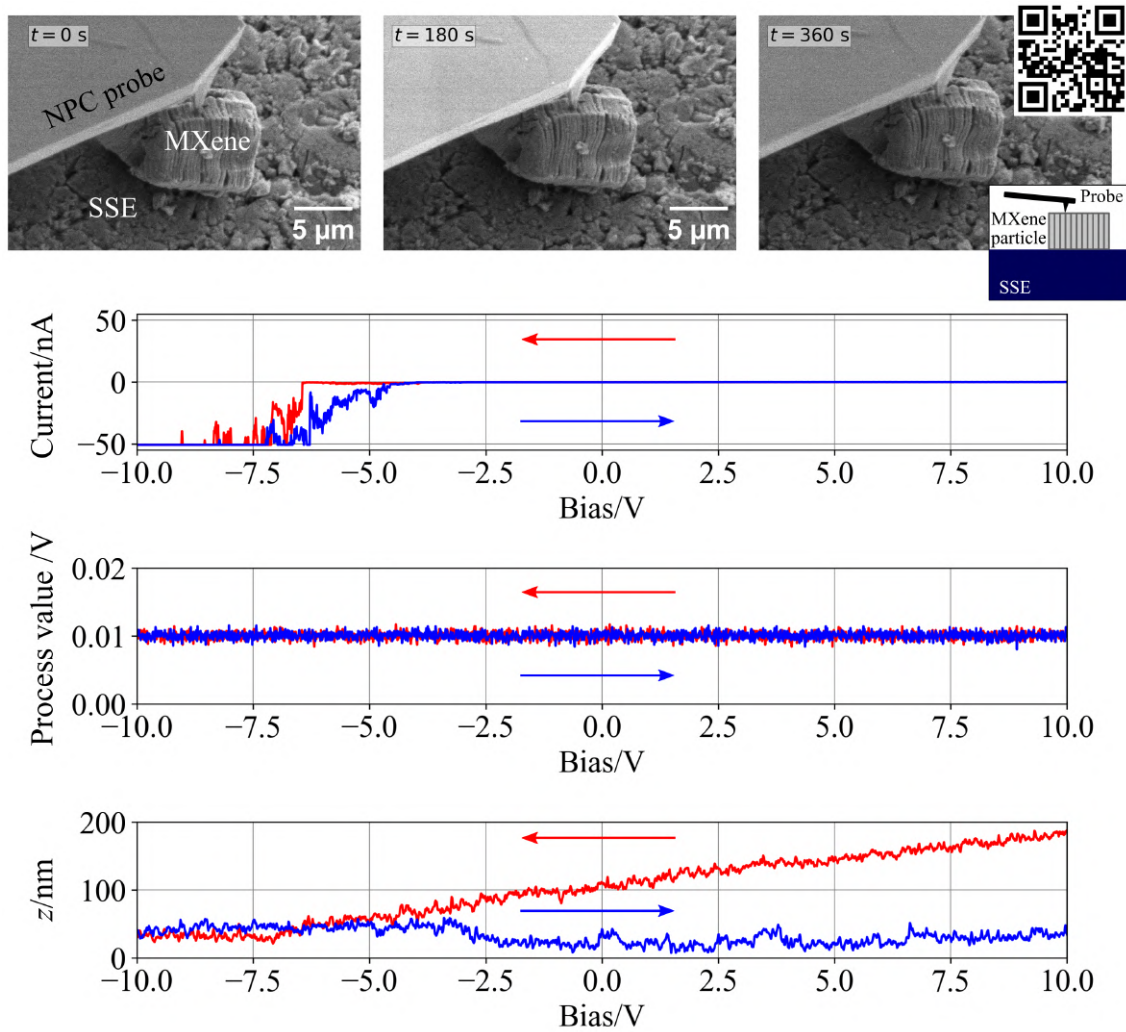# Supplement A: MXene discharging

Figure 5.1: Charging of a vertically stacked MXene particle. A wide IV sweep ($V_{sweep} = 10\,\text{V}$) was performed. The initial state is shown in the top left image, the state after the first half of the sweep (from $10\,\text{V}$ to $-10\,\text{V}$) is shown in the top middle image and the final state is shown in the top right image. The red curves show data from the first half of the sweep, and the blue curves show data from the second half. The development in the z-coordinate can be attributed to the scanner drift. The magnitude of current does not affect the z-coordinate. No correction has been applied to the z-coordinate to account for the drift. No visible change was detected by the SEM. No current was measured with positive bias on the tip in the second half of the sweep. The reason for this could be the loss of conductive contact between the tip and the particle. The images were taken by an SEM in SE detection mode at $5\,\text{kV}$. The change in contrast results from the change in probe bias that influences SEs, as they are emitted from the sample with energies below $50\,\text{eV}$ and are therefore sensitive even to the low voltage used to bias the probe. A video of the experiment is available through the QR code in the Figure or at: `https://youtu.be/49jTfubOJOk`.
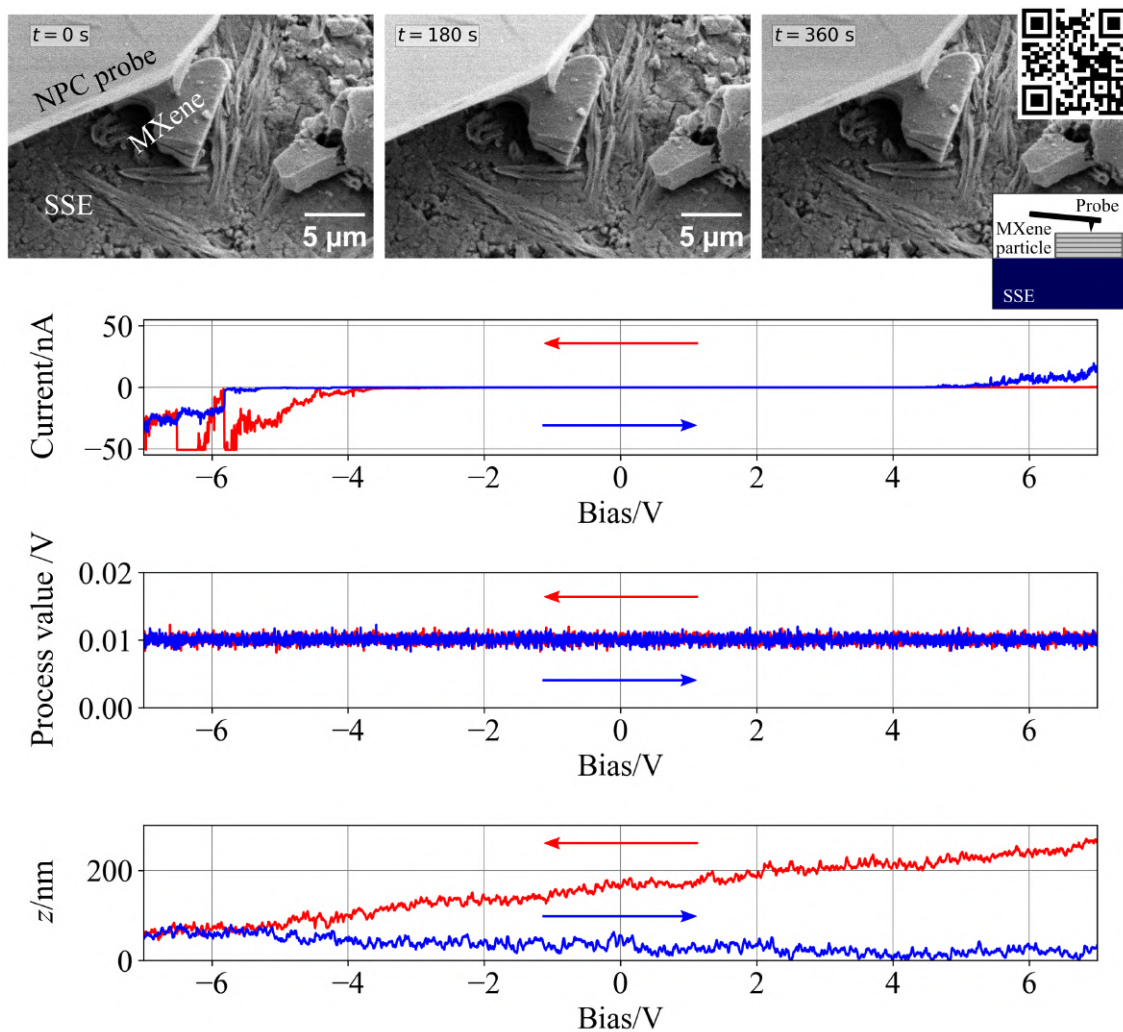
Figure 5.2: Charging of a horizontally stacked MXene particle. A wide IV sweep ($V_{sweep} = 7\,\text{V}$) was performed. The initial state is shown in the top left image, the state after the first half of the sweep (from $7\,\text{V}$ to $-7\,\text{V}$) is shown in the top middle image and the final state is shown in the top right image. The red curves show data from the first half of the sweep, and the blue curves show data from the second half. The development in the z-coordinate can be attributed to the scanner drift. The magnitude of current does not affect the z-coordinate. No correction has been applied to the z-coordinate to account for the drift. No visible change was detected by the SEM. The images were taken by an SEM in SE detection mode at $5\,\text{kV}$. The change in contrast results from the change in probe bias that influences SEs, as they are emitted from the sample with energies below $50\,\text{eV}$ and are therefore sensitive even to the low voltage used to bias the probe. A video from the experiment is available through the QR code in the Figure or at: `https://youtu.be/0aol0OVH-5o`.

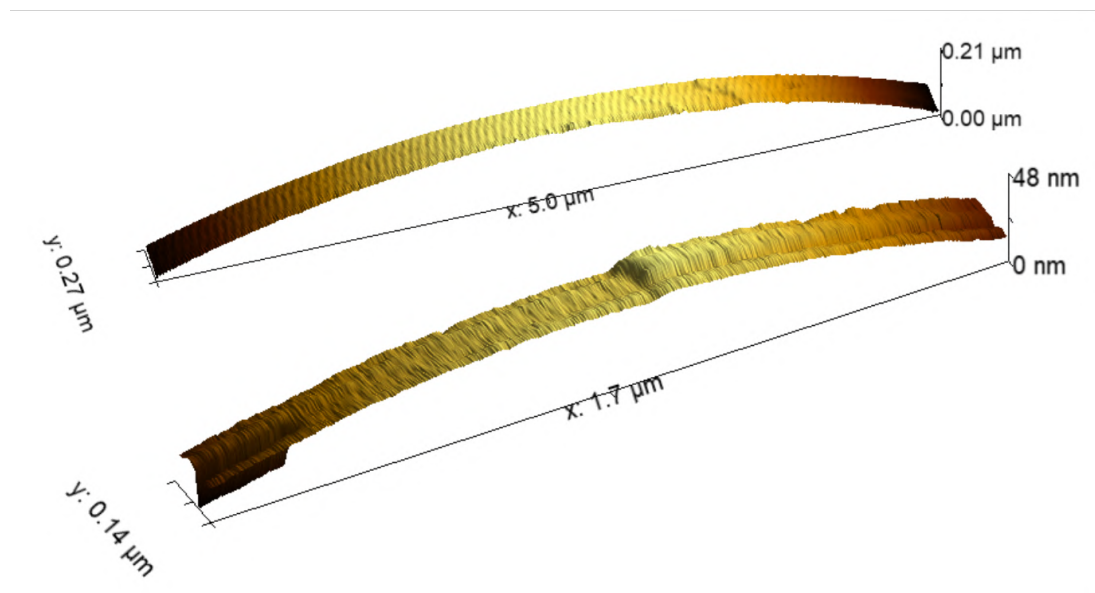# Supplement B: 3D views of graphene scans

Figure 5.3: 3D views of of scans shown in Figures 4.11 and 4.13 without the subtraction of gold sphere shape. The rows have been aligned by their median height value as this operation only shifts them by a constant value and it is necessary to remove certain microscope artefacts.